An atlas of microtubule lattice parameters regulated through ligand binding to the microtubule stabilizing sites.

Lucena-Agell, D.[1*]; Fernández, Ó.[1*]; París-Ogáyar, R.[1,2*]; Estévez-Gallego, J.[3], Ondrúšková, D.[4]; Álvarez-Bernad, B. [1]; Bonato, F. [1]; Larraga, J. [1], Ortíz de Elguea, D. [1]; Cano, G.J. [1]; Scheers, M. [1]; Imai, H. [5]; Yagi, T. [6]; Iwamoto, H.[7]; Martínez-Guil, J. C. [8]; Singh, A.J.[9]; Keyzers, R.A.[10]; Vanderwal, C. [11]; Altmann, K.-H. [12]; Van der Eycken, J. [13]; Palomo, V.[2]; Fang, W-S.[14]; Gago, F. [15]; Lánský, Z.[4]; Braun, M.[4]; Oliva, M.A.[1]; Kamimura, S.[16]; Díaz, J.F.[1]

[1]Unidad BICS, Centro de Investigaciones Biológicas Margarita Salas, Consejo Superior de Investigaciones Científicas, 28040 Madrid, Spain.

[2]Instituto Madrileño de Estudios Avanzados en Nanociencia (IMDEA-Nanociencia), Madrid, Spain.

[3]Laboratory of Biomolecular Research, Department of Biology and Chemistry, Paul Scherrer Institute, Villigen, Switzerland.

[4]Institute of Biotechnology of the Czech Academy of Sciences, BIOCEV, Prague West, Czech Republic.

[5]Department of Biological Sciences, Graduate School of Science, Osaka University, Japan.

[6]Department of Life Sciences, Faculty of Biological Resources, Prefectural University of Hiroshima, Japan.

[7]Research & Utilization Division, Japan Synchrotron Radiation Research Institute (JASRI), SPring-8, Japan.

[8]ALBA Synchrotron, CELLS, Cerdanyola del Vallès 08290, Spain.

[9]Ferrier Research Institute, and Centre for Biodiscovery, Victoria University of Wellington, PO Box 600, Lower Hutt 5010, New Zealand.

[10]School of Chemical & Physical Sciences, and Centre for Biodiscovery, Victoria University of Wellington, PO Box 600, Wellington 6140, New Zealand.

[11]Department of Chemistry, 1102 Natural Sciences II, and Department of Pharmaceutical Sciences, 856 Health Sciences Road, Suite 5400, University of California, Irvine, CA 92697, USA.

[12]ETH Zurich, Department of Chemistry and Applied Biosciences, Institute of Pharmaceutical Sciences, 8093 Zürich, Switzerland.

[13]Department of Organic and Macromolecular Chemistry, Faculty of Sciences, Ghent University, Krijgslaan 291 (S.4), B-9000 GHENT, Belgium.

[14]Institute of Materia Medica, Chinese Academy of Medical Sciences & Peking Union Medical College, 2A Nan Wei Road, Beijing 100050.

[15]Department of Biomedical Sciences, University of Alcalá, Madrid, Spain.

[16]Department of Biological Sciences, Faculty of Science and Engineering, Chuo University, Tokyo, Japan.

*These authors have contributed equally.

ABSTRACT

Microtubules (MTs) are dynamic cytoskeletal polymers whose lattice architecture regulates force generation, nucleotide hydrolysis, and recognition by motor proteins and microtubule-associated proteins (MAPs). Microtubule-stabilizing agents (MSAs), including taxanes and laulimalide/peloruside-site ligands, suppress depolymerization by binding to defined lattice sites, yet stabilization is not structurally neutral. How ligand chemistry reshapes lattice organization and function remains unresolved.

Here, we address three mechanistic questions. First, do distinct ligand classes induce defined lattice states? Using X-ray fiber diffraction, we show that MSAs selectively stabilize two preferred longitudinal conformations, a compact state (~4.06 nm monomer rise) and an expanded state (~4.17 nm), while modulating lateral organization reflected in shifts in mean MT radius. These axial spacings cluster around discrete values across chemotypes, indicating stabilization of pre-existing conformational minima rather than continuous distortion. Second, are these states interconvertible upon changes in ligand occupancy? Time-resolved diffraction reveals that longitudinal transitions occur within seconds of ligand addition even at substoichiometric occupancy; whereas, lateral equilibration proceeds slower, consistent with redistribution within heterogeneous protofilament organizations. Third, do such structural states alter nucleotide hydrolysis and motor/MAP behavior? Expanded lattices display reduced steady-state GTP hydrolysis and altered kinesin motility, whereas compact lattices preferentially promote tau binding and distinct motor interaction profiles.

Together, these findings establish longitudinal lattice conformation as a regulatory parameter and position microtubule-stabilizing agents as chemical tools that bias a dynamic structural landscape with predictable catalytic and transport consequences.

Significance statement

Microtubules generate force and support intracellular transport through lattice geometries selectively recognized by motor proteins and microtubule-associated proteins. Microtubule-stabilizing drugs such as taxanes and epothilones are widely used in chemotherapy but can cause neurotoxicity, likely because stabilization alters lattice architecture rather than simply preventing depolymerization. Here, we show that stabilizing ligands bias microtubules between two preferred longitudinal conformations - compact and expanded - that can switch within seconds of binding, while lateral organization adjusts slower. These structural states differentially regulate GTP hydrolysis and recognition by tau and kinesin, linking lattice geometry to catalytic and transport functions. By establishing lattice conformation as a tunable regulatory parameter, this work provides a framework for interpreting drug effects and designing structure-selective stabilizers with improved therapeutic profiles.

Introduction

Microtubules (MTs) are dynamic cytoskeletal polymers essential for force generation, maintenance of cell shape, and polarized intracellular transport (1). They are assembled from αβ-tubulin heterodimers, whose conformational transitions couple nucleotide hydrolysis to polymerization, enabling mechanical work. Like actin, tubulin operates through an assembly state-dependent conformational change known as the cytomotive switch (2). In tubulin, this switch involves a curved-to-straight transition characterized by interdomain rotation and displacement of helix H7 (3-5).

Because this conformational transition underlies controlled force generation, compounds that interfere with it disrupt processes such as cell division and angiogenesis. Many organisms have therefore evolved tubulin-targeting anticytomotive compounds (6), which bind to at least eight distinct sites on αβ-tubulin (7-9). Six of these sites are associated with microtubule-destabilizing agents (MDAs), including colchicine, vinblastine, maytansine, pironetin, gatorbulin, and todalam. These compounds block the cytomotive switch either by trapping tubulin in the curved conformation (e.g., colchicine, mebendazole and gatorbulin) or by disrupting longitudinal interdimer contacts (e.g., vinblastine, maytansine and pironetin), thereby preventing polymerization and collapsing the microtubule network (10-13). While highly effective against proliferating tumors, their mechanism of action involves the destruction of microtubules leading to one of the most limiting side effects in successful cancer therapy: peripheral neurotoxicity, caused by damage or degeneration of peripheral nerves (14).

Paclitaxel (Taxol®, PTX), approved in 1992 (15), inaugurated a second class of microtubule-targeting agents (MTAs): microtubule-stabilizing agents (MSAs). This group includes docetaxel (DTX), cabazitaxel (CBTX), and ixabepilone (IBP), which block the cytomotive switch in the straight-to-curved direction, thereby stabilizing polymerized MTs. Most MSAs [taxanes, epothilones, discodermolides (DDM), zampanolides (ZMP)] bind to the taxane site, reinforcing lateral contacts by stabilizing the M loop (16). In contrast, laulimalide (LAU)- and peloruside A (PLA)-site ligands stabilize MTs by bridging adjacent protofilaments (17). Although stabilization was initially thought to preserve structural roles while selectively affecting force generation, MSAs exhibit neurotoxicity comparable to destabilizing agents (18, 19).

Structural analyses reveal that stabilization is not structurally neutral. PTX and DTX induce longitudinal lattice expansion, increasing the monomer repeat from 4.06 nm to 4.17 nm and, in some cases, altering interprotofilament angles (16). In contrast, LAU-site ligands stabilize MTs without inducing axial expansion, though they may distort lateral interfaces. Notably, compounds such as pelophen B (PPH) can stabilize MTs without detectable lattice distortion (20). These observations suggest that stabilization and lattice geometry are separable properties.

MT structure also regulates its own biochemical activity. GTP hydrolysis at the β-tubulin exchangeable site, activated across the interdimer interface, establishes a nucleotide gradient along the lattice that is translated into subtle structural differences recognized by microtubule-associated proteins (MAPs) (1, 21). MAPs, including EB proteins, tau, and motors, selectively recognize specific lattice conformations. For example, kinesin-1 displays enhanced affinity for

116 expanded lattices (22), whereas tau preferentially binds compacted lattices (23). These findings
117 indicate that MAPs function as both sensors and modulators of lattice structure, and that drug-
118 induced structural distortions are likely to alter MAP behavior (24).
119 Given the clinical relevance of tubulin-targeted therapies, it is essential to understand how
120 MSAs modulate microtubule architecture and its functional consequences. Here, we
121 systematically compare multiple chemotypes targeting both stabilizing sites under identical
122 conditions. Using fiber diffraction of aligned MTs, molecular dynamics simulations, and TIRF-
123 based single-molecule assays, we define discrete lattice states and examine their kinetic and
124 functional implications for nucleotide hydrolysis and MAP interaction. This integrative framework
125 provides a structural atlas of ligand-induced lattice states and offers tools to chemically
126 manipulate microtubule architecture with precision.
127
128 **Results.**
129 ***Distinct stabilizing-site ligands induce different lattice states***
130 The objective of the present study was to determine how ligand chemistry modulates
131 microtubule architecture and function. To address this, we focused on three mechanistic
132 questions: (i) do distinct ligand classes induce defined lattice states; (ii) are these states
133 interconvertible upon changes in ligand occupancy; and (iii) do such structural states alter
134 nucleotide hydrolysis and motor/MAP behavior? The following sections address these questions
135 using complementary structural, kinetic, and functional approaches.
136 Previous work from our group demonstrated that PTX (16, 25, 26) and other taxanes (16,
137 27, 28) markedly influence microtubule (MT) architecture, affecting both longitudinal lattice
138 spacing and lateral organization. A recurring feature is lattice longitudinal expansion, reflected by
139 an increase in monomer rise from ~4.06 nm to ~4.17 nm. Similar expanded conformations have
140 been reported for hyper-stabilized MTs assembled with GMPCPP (29-31) and for catalytically
141 inactive Gluα254A and Gluα254N MTs (32). However, expansion is not universally associated
142 with activation. GMPPCP- and metal fluoride (BeF_3^- and AlF_4^-)-stabilized MTs can adopt
143 compressed states (26), and PTX- and BeF_3^--bound MTs likewise stabilize a compressed lattice
144 (26). Conversely, expansion can be induced by BIII, a PTX precursor lacking the C-13 side chain
145 and displaying minimal activity (16). Together, these observations indicate that longitudinal lattice
146 expansion reflects specific structural effects of ligand binding rather than tubulin activation *per se*.
147 To systematically define how ligand chemistry regulates MT structure, we analyzed
148 aligned MTs by X-ray fiber diffraction (33) in the presence of a broad panel of MT-stabilizing
149 agents (MSAs) targeting either the taxane or the peloruside/laulimalide sites (**Figure 1**). This
150 library comprises taxanes, epothilones, DDM, ZMPs, cyclostreptin (CSTR), taccalonolide AJ
151 (TACCA-AJ), LAU and pelorusides. Previously reported datasets (16, 20, 26, 34) were re-
152 measured or re-analyzed under identical conditions to ensure strict internal consistency across
153 the entire dataset (**Table I**). Additional conformational data obtained in the presence of γ-
154 phosphate or nucleotide analogs are presented in **Table SI**.

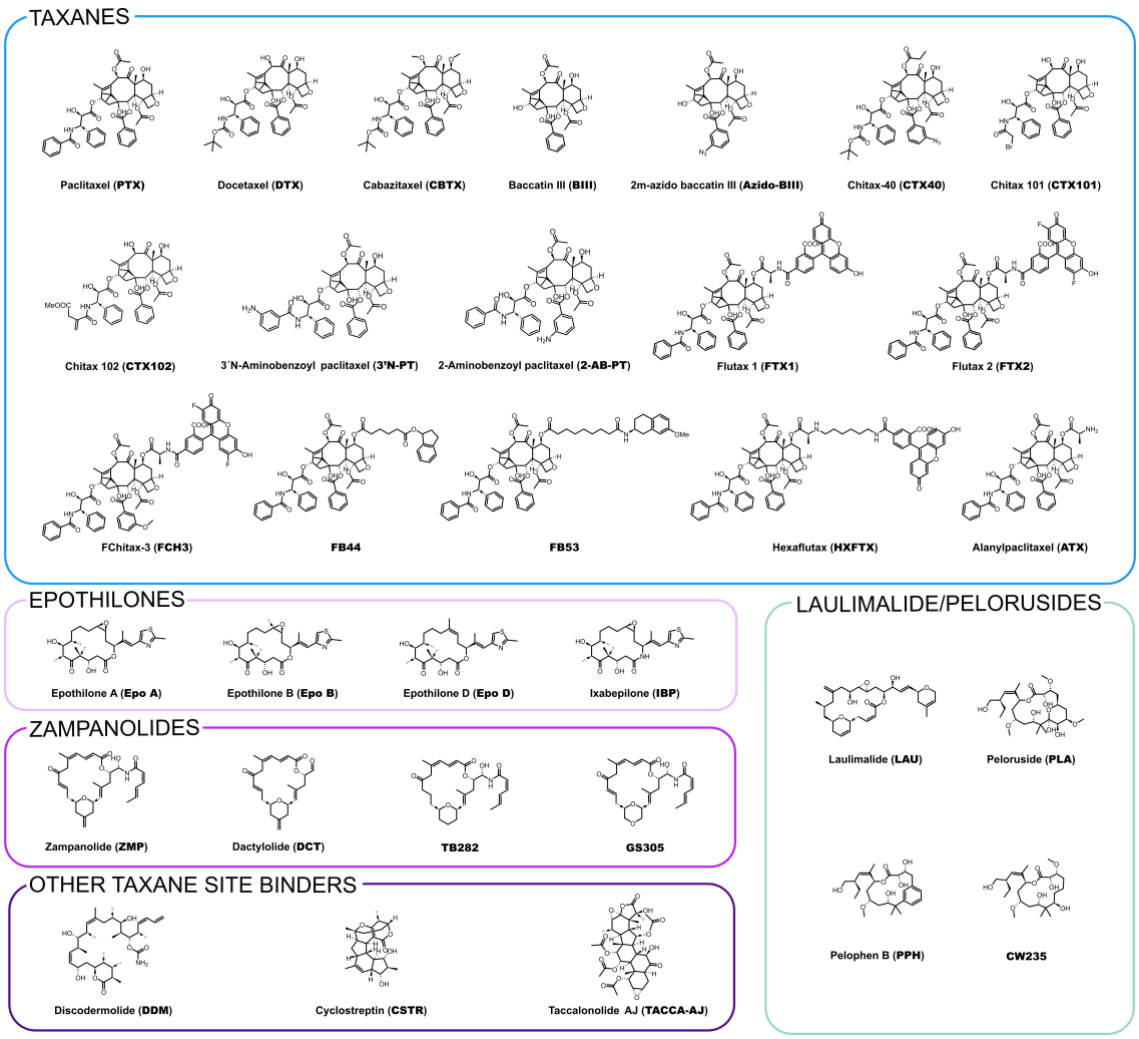

Figure 1. **Chemical structures of the microtubule-stabilizing ligands used in this study**, grouped by chemotype and binding site (taxane-site ligands and peloruside/laulimalide-site ligands).

Drug	Average Radius (nm)[1]	Estimated average PF number (model-derived)[2]	4th layer line position (nm^{-1})	Monomer rise (nm)	Lattice logitudinal state[3]
Non drug-stabilized MTs					
Apo	11.72 ± 0.01	12.9	0.987 ± 0.001	4.05 ± 0.01	C
Taxanes					
PTX	11.15 ± 0.03	12.3	0.958 ± 0.001	4.17 ± 0.02	E
DTX	11.78 ± 0.03	13.0	0.958 ± 0.001	4.17 ± 0.02	E
CBTX	11.7 ± 0.1	12.8	0.960 ± 0.001	4.16 ± 0.03	E
BIII	10.68 ± 0.01	11.8	0.958 ± 0.001	4.17 ± 0.01	E
Azido-BIII	10.63 ± 0.03	11.7	0.960 ± 0.001	4.17 ± 0.01	E
CTX40	11.50 ± 0.05	12.7	0.958 ± 0.001	4.18 ± 0.01	E
CTX101	11.47 ± 0.04	12.6	0.950 ± 0.004	4.21 ± 0.02	E
CTX102	11.45 ± 0.02	12.6	0.960 ± 0.001	4.16 ± 0.01	E
3´N-PT	11.15 ± 0.06	12.3	0.956 ± 0.002	4.18 ± 0.01	E
2-AB-PT	11.30 ± 0.04	12.5	0.957 ± 0.001	4.18 ± 0.01	E
FTX1	12.79 ± 0.02	14.1	0.989 ± 0.001	4.04 ± 0.01	C
FTX2	12.81 ± 0.06	14.1	0.986 ± 0.001	4.06 ± 0.01	C
FCH3	12.96 ± 0.03	14.3	0.983 ± 0.001	4.07 ± 0.01	C
FB44	12.58 ± 0.06	13.9	0.986 ± 0.004	4.06 ± 0.02	C
FB53	11.92 ± 0.03	13.1	0.987 ± 0.002	4.05 ± 0.01	C
HXFTX	12.68 ± 0.02	14.0	0.99 ± 0.01	4.06 ± 0.01	C
ATX	12.3 ± 0.5	13.6	0.988 ± 0.001	4.05 ± 0.01	C
Epothilones					
Epo A	11.13 ± 0.01	12.2	0.960 ± 0.001	4.17 ± 0.01	E
Epo B	11.48 ± 0.03	12.7	0.962 ± 0.002	4.16 ± 0.01	E
Epo D	11.29 ± 0.04	12.4	0.966 ± 0.006	4.15 ± 0.03	E
IBP	11.24 ± 0.01	12.4	0.961 ± 0.001	4.16 ± 0.01	E
Zampanolides					
ZMP	13.17 ± 0.03	14.5	0.988 ± 0.001	4.05 ± 0.02	C
DCT	11.77 ± 0.01	13.0	0.959 ± 0.001	4.17 ± 0.01	E
TB282	10.5 ± 1.1	11.5	0.987 ± 0.001	4.05 ± 0.01	C
GS305	13.18 ± 0.02	14.5	0.987 ± 0.001	4.05 ± 0.01	C
Discodermolide					
DDM	11.7 ± 0.4	12.9	0.988 ± 0.003	4.05 ± 0.02	C
Cyclostreptin and Taccalonolide					
CSTR	11.77 ± 0.03	13.0	0.987 ± 0.001	4.05 ± 0.01	C
TACCA-AJ	11.58 ± 0.03	12.8	0.987 ± 0.001	4.05 ± 0.01	C
Peloruside/Laulimalide					
LAU	12.47 ± 0.03	13.8	0.990 ± 0.003	4.04 ± 0.02	C
PLA	10.83 ± 0.03	11.9	0.987 ± 0.001	4.05 ± 0.01	C
PPH	11.74 ± 0.03	12.9	0.987 ± 0.001	4.05 ± 0.01	C
CW235	11.90 ± 0.04	13.1	0.987 ± 0.001	4.05 ± 0.01	C
Co-Stabilized Microtubules					
PTX+LAU	12.19 ± 0.03	13.4	0.958 ± 0.001	4.17 ± 0.01	E
PTX+PLA	10.42 ± 0.03	11.5	0.954 ± 0.001	4.19 ± 0.01	E

Table I. **Structural parameters of microtubules in the presence of stabilizing ligands**.

1.- Reported SEM values correspond to the uncertainty in the determination of the mean microtubule radius from diffraction measurements and do not reflect the dispersion of protofilament numbers within the heterogeneous microtubule population.
2.- Protofilament (PF) numbers were estimated from the measured mean MT radius using a geometric conversion [assuming an average inter-protofilament distance of 5.7 nm (27)] and are provided for comparative purposes only. Throughout the manuscript, longitudinal spacing and mean radius are treated as primary observables, whereas PF number serves as a derived descriptor of lateral organization within heterogeneous MT populations. Protofilament numbers are therefore rounded to the nearest decimal.
3.- Lattice longitudinal state classification: C, compressed lattice; E, expanded lattice.

173 Fiber diffraction patterns revealed two principal structural effects of ligand binding (**Figure**
174 **2, Figure S1**). First, several ligands induce a clear shift in longitudinal lattice spacing, consistent
175 with previous observations (26, 35). This shift is visible as an inward displacement of the
176 meridional layer lines arising from the helical repeat (located at 1/4, 2/4, 3/4 and 4/4 nm^{-1} in the
177 diffractogram; see Materials and Methods) (**Figures S1C–H**), corresponding to an increase in
178 monomer rise from ~4.06 nm (compressed state) to ~4.17 nm (expanded state). The expansion
179 is asymmetric, and a reflection at ~1/8 nm^{-1} becomes detectable, consistent with the emergence
180 of the full ~8 nm axial periodicity of the αβ-tubulin dimer. Across the analyzed ligands, the
181 longitudinal spacing clustered around these two preferred values, consistent with two
182 interconvertible longitudinal lattice states rather than broad continuous variation. Notably, under
183 some co-stabilization conditions, specifically GMPCPP-stabilized microtubules bound to ligands
184 that favor compression, intermediate or broadened layer lines were observed, indicative of
185 structural heterogeneity within the MT population (**Table SI**).
186 The axial spacing measured by fiber diffraction (~40–42 Å) corresponds to half of the αβ-
187 tubulin dimer repeat and is therefore consistent with the ~81–84 Å dimer rise reported by cryo-
188 EM. The apparent discrepancy arises because α- and β-tubulin are not individually resolved at
189 the resolution of the diffraction experiment, whereas they are distinguished in cryo-EM
190 reconstructions. Accordingly, the ~1/4 nm^{-1} meridional reflection reports the monomer repeat,
191 while the full dimer periodicity appears at ~1/8 nm^{-1}. This latter reflection is prominent in expanded
192 lattices but weak or absent in compressed lattices (**Figure S1**), indicating that the longitudinal
193 conformational change is largely asymmetric within the αβ-tubulin dimer.
194 Second, ligand binding modulates lateral lattice geometry, reflected through shifts in the
195 position of the equatorial maxima of the diffractograms (**Figure S1G**). These changes correspond
196 to variations in mean MT radius and lateral inter-protofilament organization within heterogeneous
197 *in vitro*–assembled populations that contain a distribution of protofilament numbers. This is
198 consistent with previous observations for both the taxane site (25, 27) and the
199 peloruside/laulimalide site (20).
200 A consistent relationship between longitudinal and lateral parameters is observed: ligands
201 that stabilize expanded lattices tend to maintain or slightly reduce the mean MT radius; whereas,
202 compounds that preserve compressed axial spacing are frequently associated with increased
203 mean radius. For example, BIII stabilizes an expanded lattice while reducing mean radius, while
204 ZMP stabilizes a compressed lattice with increased mean radius (**Figure 2 and Table I**).
205 Combinations of drugs with GMPCPP further illustrate this decoupling, resulting in MT populations
206 with increased mean radius while maintaining an expanded longitudinal lattice (**Table SI**).
207 Importantly, not all taxane-site ligands induce lattice expansion. While most taxanes,
208 except those modified at C-7 (34), and epothilones promote expansion, DDM, ZMP, CSR,
209 TACCA-AJ, and ligands targeting the peloruside/laulimalide site stabilize MTs without altering
210 axial spacing, in agreement with previous observations (20). These findings indicate that
211 stabilization through the taxane site can be mechanistically separable from longitudinal lattice
212 expansion.

Collectively, these results address the first mechanistic question by showing that ligand binding stabilizes defined lattice states, characterized by two preferred longitudinal conformations and ligand-dependent lateral organization. Notably, lattice state depends on specific chemical features rather than binding site alone, as closely related taxanes (including C-7-modified analogues) stabilize distinct conformations.

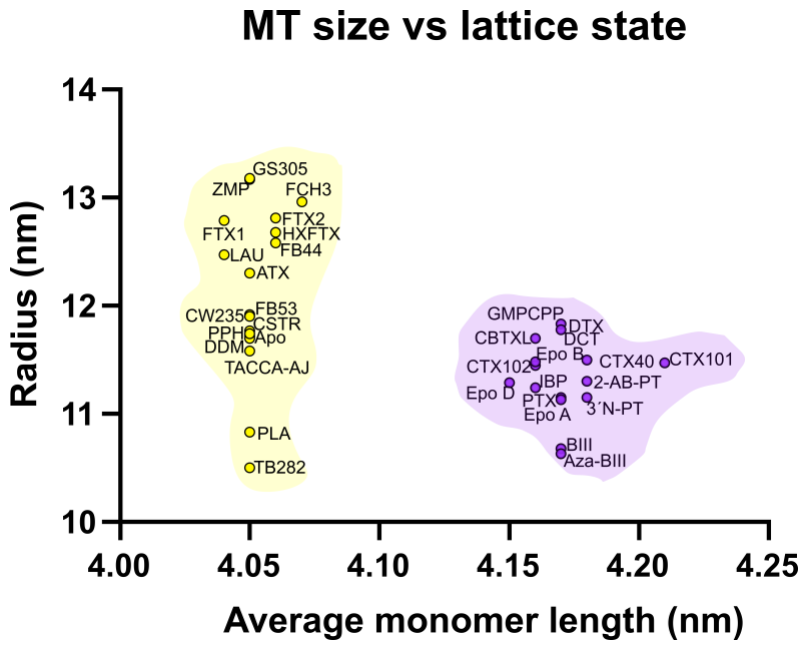

Figure 2. Relationship between the MT lattice expansion state and MT radius for all the measured conditions.

Stoichiometry of the taxane site regulation of the microtubule structure.

Having established that occupancy of the taxane site alters longitudinal lattice spacing and lateral geometry, we next examined the ligand:tubulin stoichiometry required to induce these structural transitions (**Figure 3**). This analysis provides insight into how partial site occupancy, more relevant to cellular conditions, modulates lattice organization.

Five taxane-site ligands were selected: clinically used compounds PTX (**Figure 3A**), DTX (**Figure 3B**), and IBP (**Figure 3C**), a minimally modified fluorescent taxane derivative (3′N-PT) (**Figure 3D**), and the covalent binder ZMP (**Figure 3D**). PTX, IBP, and 3′N-PT induce lattice expansion and modifies mean radius; DTX which primarily modulates longitudinal spacing; and ZMP, which stabilizes a compressed lattice, was tested on pre-expanded GMPCPP-bound MTs.

Remarkably, lattice expansion was observed at substoichiometric ligand:tubulin ratios. For all expanding compounds tested, the longitudinal spacing approached that of the fully ligand-bound state at partial occupancy, typically around a 1:3–1:2 ratio. In contrast, ZMP induced re-compression of GMPCPP-expanded MTs but required near-stoichiometric occupancy to achieve this effect.

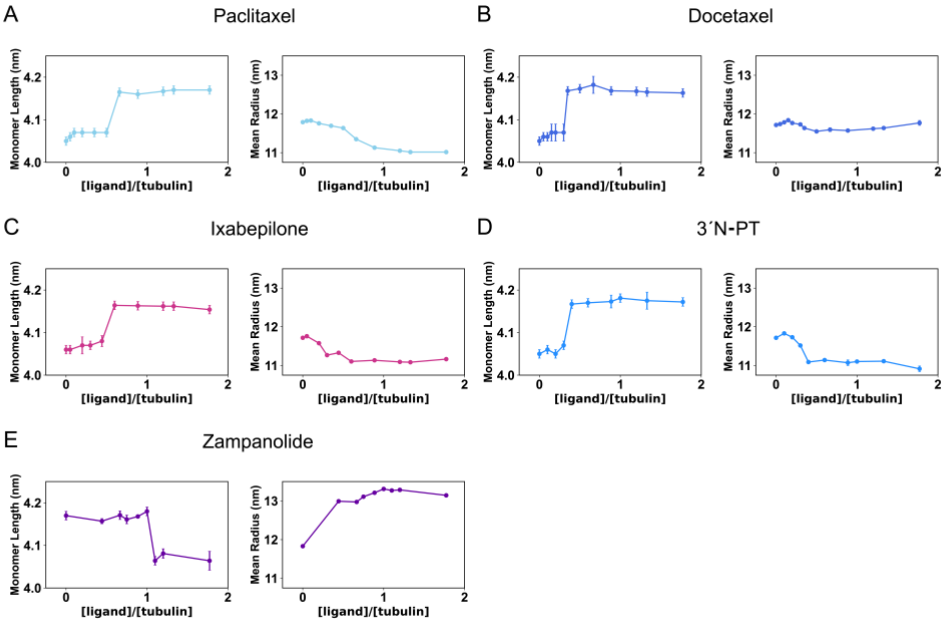

Figure 3. Structural response of apo- (compressed A, B, C, D) and GMPCPP- (expanded, E) microtubules to different ligand:tubulin ratios. The plots show the variation in average monomer length and mean radius, highlighting the impact of ligand concentration on lattice organization. (A) PTX, (B) DTX, (C) IBP, (D) 3´N-AB-PT, (E) ZMP.

Importantly, the longitudinal response did not vary continuously with ligand concentration but clustered around the compressed (~4.06 nm) or expanded (~4.17 nm) states. Intermediate axial spacings were not resolved within experimental uncertainty. In contrast, lateral changes in mean radius did not display an equally sharp transition, consistent with the heterogeneous distribution of protofilament numbers in *in vitro*–assembled MT populations. These findings indicate that partial occupancy of the taxane site is sufficient to bias the MT lattice toward defined structural states, consistent with a cooperative structural response of the polymer.

Time-resolved fiber diffraction analysis of the structural effect of chemical stabilization of microtubules induced by MSAs.

Having defined the stoichiometry required to induce structural transitions, next we examined how pre-formed MT lattices respond to acute changes in chemical environment (**Supp. Movie 1**). We analyzed three taxane-site ligands: DTX (minimal effect on mean radius), PTX, and BIII (both associated with reduced mean radius at equilibrium) - all of which stabilize expanded lattices - and compared them with laulimalide, which increases mean radius without altering axial spacing (20). Previous time-resolved measurements of non-aligned MTs showed that diameter changes following PTX or DTX addition occur within the ~30 s dead time of the technique (36). Using a shear-flow mixing system with ~1 s resolution, we independently monitored axial and radial parameters (**Figure 4**).

Upon addition of PTX, DTX, or BIII, axial lattice expansion was detected within the first second of measurement. In all cases, the monomer rise shifted rapidly toward the expanded value (~4.17 nm). Because this axial parameter is determined directly from meridional peak positions and does not rely on geometric modeling, these observations indicate that longitudinal lattice rearrangement occurs on a sub-second timescale. In contrast, addition of LAU, which does not alter axial spacing, produced no detectable change in monomer rise (**Figure 4D**), serving as an internal control.

The radial response differed markedly. Although equilibrium measurements indicate substantial differences in mean radius between apo- and drug-stabilized MTs (**Table I**), early time-resolved changes in mean radius were significantly smaller. For example, PTX-stabilized MTs assembled in the continuous presence of the drug exhibit, on average, ~0.6 nm smaller radius than apo MTs (**Table I**), yet only a ~0.3 nm decrease was measured within the first 3 s following addition to pre-assembled MTs. Similarly, BIII, associated with a larger equilibrium reduction (~1.0 nm), produced only a modest early shift. Conversely, LAU produced a modest early increase (~0.3 nm) in mean radius, consistent with its known equilibrium effect (20). Control experiments in which apo assembled microtubules were incubated (30 min) with superstoichiometric concentrations of PTX, DTX and BIII mean radius do not completely shift towards the values of those assembled in the presence of the drug (11.28 nm vs 11.15 nm for PTX, 11.02 nm vs 10.68 nm for BIII) (**Table S2**) indicating that full equilibration of lateral organization requires substantially longer times.

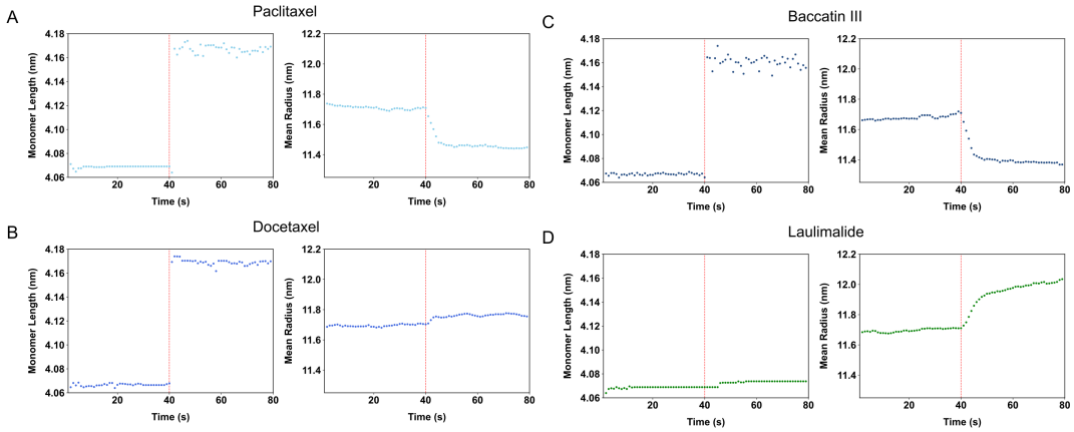

Figure 4. Time-resolved axial and radial measurements reveal different dynamics of microtubule lattice reorganization after ligand addition at 40 s (red dashed line). Left: average axial tubulin repeat. Right: average mean radius. Ligands: (A) PTX, (B) DTX, (C) BIII, (D) LAU.

Importantly, the magnitude of the rapid radial change was consistently smaller than the equilibrium difference observed under steady-state conditions (**Table S2**). These results indicate that early structural responses primarily reflect rapid longitudinal lattice rearrangement, whereas changes in mean radius evolve more gradually. Given the heterogeneous nature of *in vitro*–assembled MT populations, the time-resolved fast radial shifts are consistent with rapid assembly of free tubulin available (around 15%) and not with synchronous protofilament addition or loss.

The rapid and concentration-dependent transition of the longitudinal parameter toward the expanded state, even at partial occupancy, is consistent with a cooperative structural response of the polymer lattice, in which ligand binding at a subset of sites biases the conformational equilibrium of neighboring tubulin subunits. In contrast, the slower evolution of mean radius suggests that lateral reorganization to the equilibrium state proceeds through progressive redistribution within the existing protofilament population rather than an immediate, concerted structural rearrangement.

Together, these findings address the second mechanistic question by demonstrating that ligand-induced lattice states are interconvertible, rapidly in the longitudinal dimension, whereas lateral equilibration toward the final structural distribution occurs on a longer timescale.

Molecular modeling and dynamics of ligand-modulated lattice states

To gain structural insight into how taxane-site ligands modulate lattice parameters and influence catalytic geometry, we performed normal mode analysis and molecular dynamics (MD) simulations on representative compacted and expanded microtubule interfaces. We examined (i) low-frequency collective motions in 13- and 14-protofilament lattice fragments, (ii) the conformational behavior of β1:α2 interdimer interfaces in apo and drug-bound systems (DTX, Epo A, ZMP, DDM, and ATX), and (iii) minimal three-protofilament lattice models as previously described (37). Representative compacted and expanded MT turns have been deposited in the ModelArchive repository (38) (codes listed in Materials and Methods).

Normal mode analysis consistently identified a dominant low-frequency collective motion corresponding to cooperative bending and longitudinal closure of the lattice (**Supp. Movie 2**). Sampling along this mode generated conformations consistent with subtle variations in axial rise and curvature, supporting the experimentally observed sensitivity of longitudinal spacing and mean radius to small structural fluctuations.

Comparison of β1:α2 interfaces in GTP- versus GDP-bound states reproduced the expected differences in γ-phosphate coordination and hydrogen-bonding networks at the E-site. The simulations revealed that the interdimer interface is structurally plastic and capable of sampling closely related conformational states distinguished by coordinated rearrangements of side chains, nucleotide phosphates, and associated water molecules (**Figure S2**).

When ligands were included at the taxane site, compacted and expanded lattices exhibited distinct interdimer rise distances (approximately 40.5 Å and 42.0 Å, respectively), in agreement with diffraction measurements. Ligand binding altered the conformational ensemble of the β1:α2 interface and modified the dynamic coupling between the taxane pocket and the nucleotide-binding interface. These changes were accompanied by subtle rearrangements of the hydrogen-bond network and phosphate geometry at the E-site, consistent with the experimentally observed modulation of GTP hydrolysis.

Together, these simulations show that ligand binding stabilizes distinct conformational ensembles of the interdimer interface, linking longitudinal lattice spacing to local remodeling of catalytic-site geometry.

335 ***Effect of microtubule structure on nucleotide hydrolysis.***

336 Because ligand binding modulates longitudinal lattice spacing, we examined whether
337 defined lattice states are associated with differences in GTP hydrolysis at the E-site of β-tubulin,
338 which becomes catalytically activated upon incorporation into the microtubule lattice through
339 Gluα254 of the incoming α-tubulin subunit (39).

340 First, we verified that drug-stabilized microtubules retain GTPase activity by analyzing
341 nucleotide content in assembled polymers. After one hour of incubation, all drug-bound MTs
342 contained approximately one mole of GTP and one mole of GDP per tubulin dimer, consistent
343 with continued GTP hydrolysis under the experimental conditions.

344 We next quantified steady-state GTP hydrolysis of MTs in the presence of expanding
345 ligands (PTX, Epo A) and non-expanding ligands bound to either the taxane site (DDM, ZMP) or
346 the peloruside/laulimalide site (PPH) (20), relative to undrugged MTs, using the malachite green
347 assay (**Table II**). As described in the Methods & Materials, phosphate accumulation was
348 measured after acid quenching and therefore reflects cumulative GTP hydrolysis associated with
349 polymerized tubulin. Because the reaction was quenched under strongly denaturing conditions,
350 the assay quantifies total inorganic phosphate generated at the time of sampling rather than
351 phosphate release kinetics.

Condition	Steady-state GTP hydrolysis rate (min^{-1})
Apo (C)	0.11 ± 0.02
PTX (E)	0.07 ± 0.01
Epo A (E)	0.07 ± 0.02
ZMP (C)	0.11 ± 0.03
DDM (C)	0.16 ± 0.02
PPH (C)	0.10 ± 0.02

352
353 **Table II**. **Steady-state GTPase hydrolysis rate of drugged expanded and compressed**
354 **microtubules**. (C) compressed and (E) expanded state of tubulin.
355

356 Expanded lattices stabilized by PTX or Epo A exhibited reduced hydrolysis rates relative
357 to apo MTs (~35% decrease). In contrast, compressed lattices stabilized by ZMP or PPH
358 displayed rates similar to apo MTs, while DDM-bound MTs showed increased hydrolysis (~45%
359 increase). Thus, modulation of longitudinal lattice state correlates with systematic differences in
360 steady-state GTPase activity.

361 Because E-site catalysis is highly sensitive to the geometric arrangement of catalytic
362 residues, nucleotide phosphates, and associated water molecules (40), these differences are
363 consistent with subtle structural changes propagated from the ligand-binding pocket to the
364 catalytic interface.

365

366 ***Effect of structural changes on chemical transport on microtubules.***

367 Kinesin-driven intracellular transport along microtubules, essential for neurotransmitter
368 trafficking in axons, is a major cellular function of the microtubule cytoskeleton (41). This process
369 depends on mechanochemical coupling between kinesin stepping dynamics and recognition of

the microtubule lattice. Having established tools to modulate microtubule structure, we next examined how defined lattice states affect kinesin-1 motility.

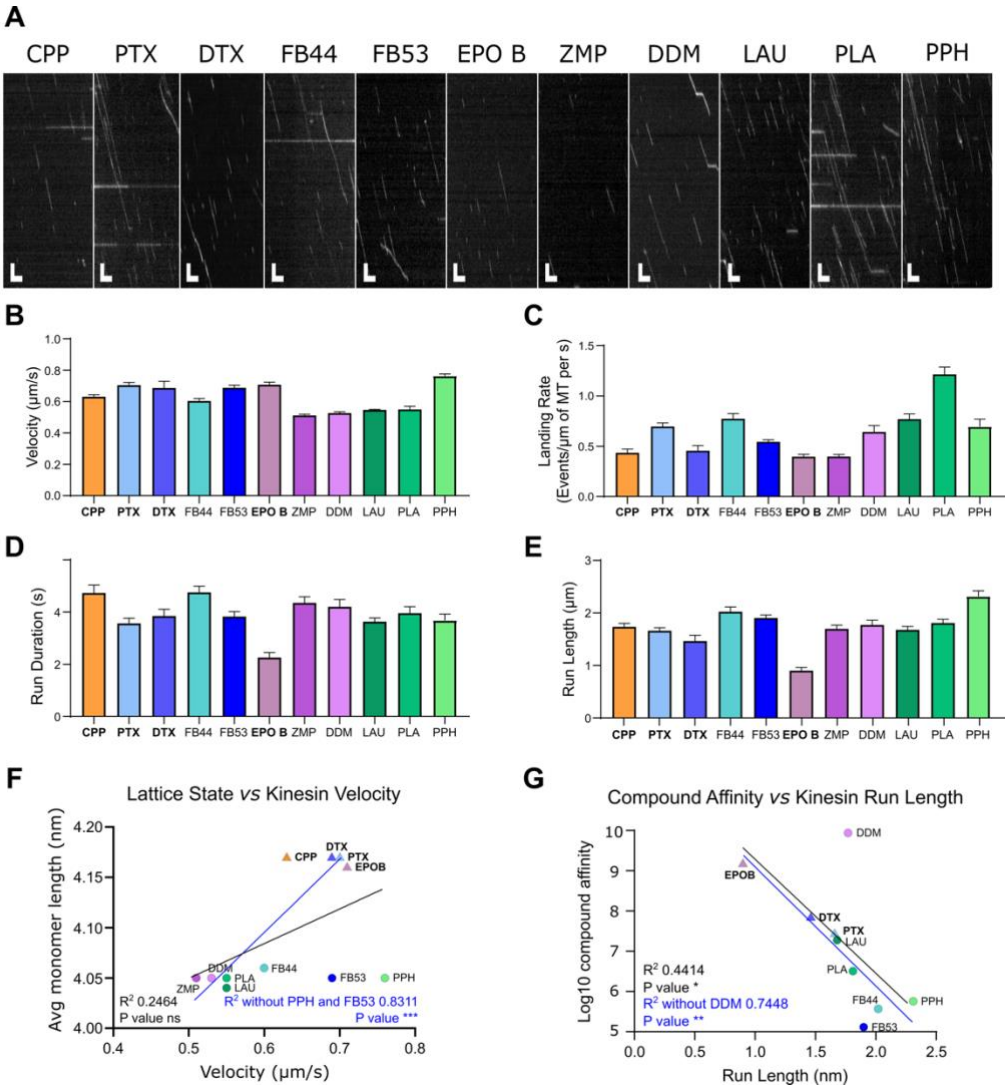

Figure 5. Characterization of kinesin motility. A. Representative kymographs of single Kif5B-eGFP motors moving along a stabilized microtubule. Vertical scale bar: 2 µm; horizontal scale bar: 10 s. **B–E.** Bar plots and quantitative summary from at least three independent experiments, showing (B) mean velocity (µm/s), (C) mean landing rate of kinesin (events/µm of MT per s), (D) mean run duration (s), and (E) mean run length (µm), of single Kif5B-eGFP molecules moving on stabilized MTs. Error bars represent the SEM. Data were pooled from ≥ 2 experiments per condition, analyzing between 36–48 MTs per replica. **F-G.** Statistical correlations found between the structural and affinity parameters of the drug-stabilized lattices and the interaction of kinesin with them**.** Pearson correlation was obtained using GraphPad Prism 8 software to determine R square and P value (**** $p < 0.0001$; *** $p < 0.001$, ** $p < 0.01$ and * $p < 0.05$). Compound binding affinities were taken from (20, 34, 43-45).

To address this question, we employed the time-lapse total internal reflection fluorescence (TIRF) microscopy system described previously (34). Using fluorescently labeled kinesin motors (Kif5B 1–905–eGFP (42)), we tracked individual motors moving along immobilized MTs stabilized by a panel of distinct MSAs that generate different lattice architectures (**Figure 5 and Supp. Movie 3**). We quantified landing rate (events per µm of MT per second), run duration, run length, and velocity.

391 Data for PTX (expanded), FTX2 (compressed), FB44 (compressed), FB53 (compressed),
392 and GMPCPP (expanded) were taken from our earlier work (34). We extended the analysis to
393 additional taxane-site ligands, DTX (expanded), Epo B (expanded), ZMP (compressed), and DDM
394 (compressed), as well as peloruside/laulimalide-site ligands: PLA, LAU, and PPH (all
395 compressed).
396 Although kinesin-MT interactions show compound-specific complexity, several consistent
397 trends emerge. Kinesin velocity exhibits a clear dependence on longitudinal lattice state (**Figures**
398 **5B, 5F**), with higher velocities consistently observed on expanded microtubules. In contrast,
399 compressed lattices display a broader distribution of velocities. Within this group, slower velocities
400 are generally associated with ligands of higher binding affinity (e.g., ZMP, DDM, LAU, PLA) (20,
401 43-45), whereas compressed lattices stabilized by lower-affinity ligands (e.g., FB44, FB53, PPH)
402 support faster movement. Thus, while expanded lattices consistently support higher kinesin
403 velocities, compaction alone does not determine stepping speed; ligand-specific effects contribute
404 to the observed variability.
405 Landing rate (**Figure 5C**) is reduced on expanded lattices and in the presence of ZMP.
406 Run duration (**Figure 5D**) is largely similar across conditions, with the exception of Epo B, which
407 produces significantly shorter dwell times. Run length (**Figure 5E**) remains relatively stable, with
408 two notable deviations: Epo B reduces run length, whereas PPH increases it. Interestingly, run
409 length shows partial correlation with ligand binding affinity (**Figure 5G**), suggesting that stronger
410 lattice stabilization may limit the local conformational adjustments required during kinesin
411 stepping.
412 Epo B is notable in that it strongly stabilizes an expanded lattice ($K_b = 1.5 \times 10^9\ M^{-1}$ at 26
413 °C) (43). Despite maintaining high stepping velocity, kinesin exhibits reduced interaction time and
414 shorter run length on Epo B-stabilized lattices, indicating that lattice expansion alone does not
415 predict motor processivity.
416
417 ***Effect of structural changes on tau binding and kinetics.***
418 Tau is the principal microtubule-associated protein in axons and requires dynamic
419 interaction with microtubules (MTs) to exert its stabilizing and protective function (46). Impaired
420 tau-MT interaction contributes to neurofibrillary tangle formation in Alzheimer's disease and
421 compromises axonal MT stability. To determine how specific lattice states influence tau
422 recognition, we analyzed the binding of mCherry-labeled tau (441 isoform) to stabilized MTs using
423 the same TIRF microscopy platform employed for kinesin assays (34).
424 Distinct ligand-stabilized MTs were immobilized in flow chambers and visualized by TIRF
425 microscopy (**Figure 6A**). Tau–mCherry binding was examined at 5 nM, 10 nM, and 40 nM (**Figure**
426 **6B–C**). ZMP, DDM, PLA, and LAU were analyzed at all three concentrations, whereas the
427 remaining ligands were tested at 10 and 40 nM. Binding was monitored over time, and both spatial
428 coverage along MT length and integrated fluorescence intensity per micron were quantified.

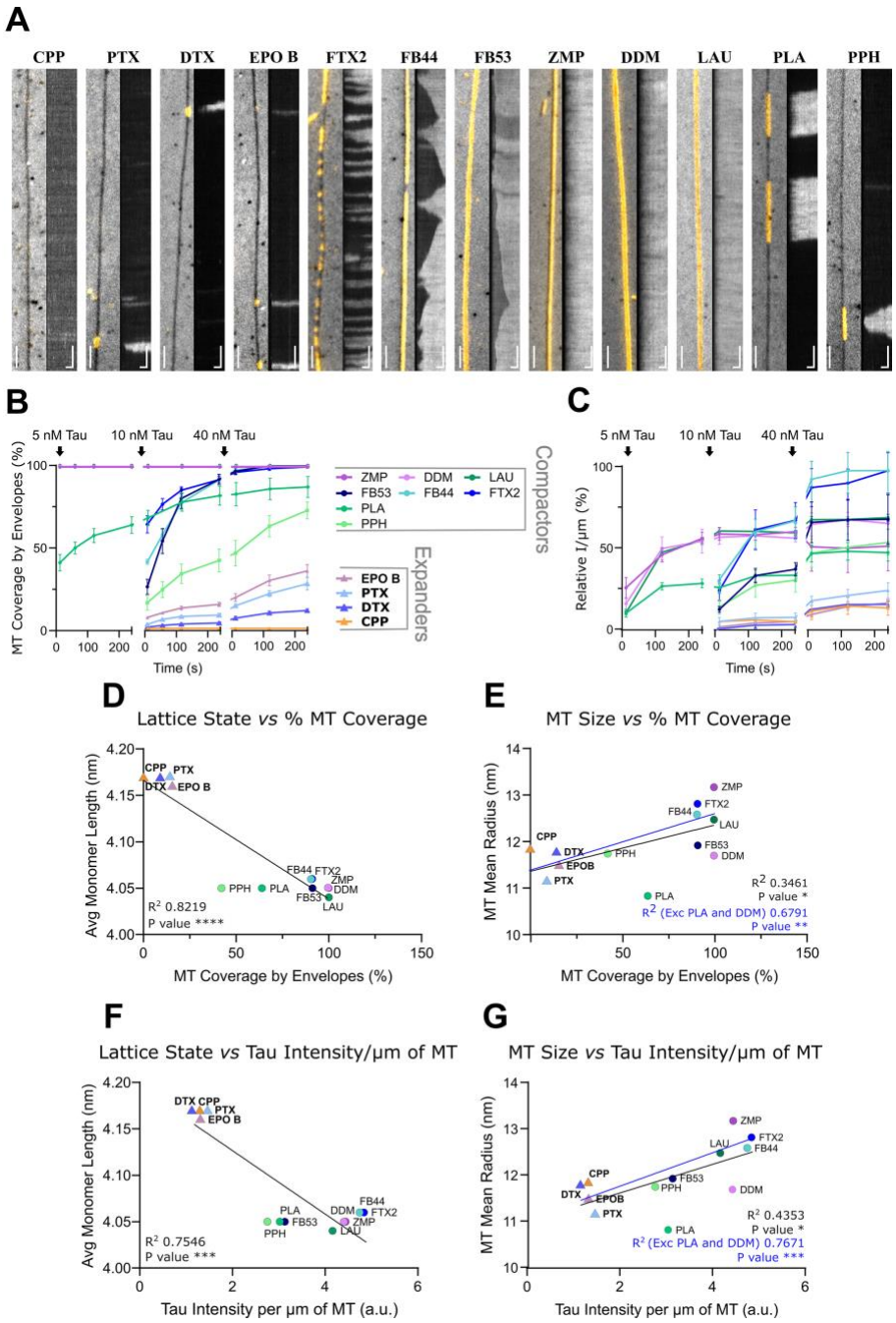

Figure 6. Characterization of tau interaction with microtubules. A. Representative fluorescence images (after 4 minutes) and corresponding kymographs of tau-mCherry binding to MTs stabilized with GMPCPP or different drugs. Vertical scale bars: 2 µm; horizontal scale bars: 60 s. Taxol derivatives are shown in blue shades, other taxanes in purple tones, and peloruside/laulimalide site ligands in different greens. Triangle symbols indicate expanders; circle symbols represent non-expander compounds. **B.** Fraction of MT length covered by tau envelopes over time following tau-mCherry addition. **C.** Integrated fluorescence density per µm of MT over time after tau-mCherry addition. **D-G.** Statistical correlations found between the structural parameters of the drug stabilized lattices and the binding of tau to them. Pearson correlation was obtained using GraphPad Prism 8 software to determine R square and P value (**** $p < 0.0001$; *** $p < 0.001$, ** $p < 0.01$ and * $p < 0.05$).

Tau binding patterns correlated strongly with longitudinal lattice state (**Figures 6D** and **6F**), and four distinct recognition behaviors were observed. First, compact lattices stabilized by

ZMP, DDM, and LAU were recognized extremely rapidly and became homogeneously coated along their entire length (**Figure 6B; Supp. Movies 4–6**). Even at 5 nM tau, near-complete spatial coverage was reached within ~10 s (the dead time of the assay), without detectable patch formation. Although total fluorescence continued to increase over time, spatial coverage was essentially immediate, indicating rapid uniform recognition followed by progressive occupancy. Second, other compact lattices (PLA, PPH, FB44, FB53, FTX2) also supported rapid tau binding (**Figure 6B**) but through a spatially heterogeneous mechanism. Binding initiated in high-density patches that grow progressively along the MT (**Supp. Movies 7–8**), consistent with cooperative envelope formation (47, 48). Recognition was therefore favorable, but spatial propagation required local reorganization. Third, GMPCPP-stabilized MTs, constrained in an expanded conformation, exhibited negligible tau binding under these conditions (**Figure 6B**), indicating that this lattice state is poorly recognized by tau. Fourth, MTs stabilized by expanding ligands (PTX, DTX, Epo B) bound tau more slowly and predominantly through patch formation (**Figure 6B; Supp. Movies 9–10**). These expanded lattices required higher tau concentrations and longer incubation times to reach substantial coverage.

Integrated fluorescence measurements were consistent with these spatial observations (**Figure 6C**): compact lattices accumulated tau rapidly, whereas expanded lattices required higher concentrations and longer times to reach comparable signal intensity. Although ZMP-, DDM-, and LAU-stabilized MTs achieved rapid spatial coverage, total fluorescence continued to increase until equilibrium, indicating that uniform coverage does not imply instantaneous maximal occupancy.

A modest correlation between mean MT radius and total tau binding was detected (**Figure 6E** and **6G**). However, longitudinal lattice state was a stronger determinant of tau recognition pattern and binding kinetics than radius alone.

Finally, we performed numerical simulations of a single-step association reaction under conditions in which tau binding proceeds without detectable lattice rearrangement, namely on ZMP-, DDM-, and LAU-stabilized microtubules. Using derived experimentally concentrations (5 nM tau; 12.5 nM accessible binding sites), binding can be modeled (**Figure S3**) as a homogeneous one-step interaction. Under these conditions, both free tau and free binding sites decrease during the reaction, and the system does not follow strict pseudo-first-order kinetics (49). Simulations reproduce the experimentally observed rapid spatial decoration followed by a slower approach to equilibrium when association rate constants on the order of a few $\mu M^{-1}\ s^{-1}$ and dissociation rate constants on the order of $10^{-3}\ s^{-1}$ (dissociation half-times of several minutes). A previous washout study of tau dissociation from PTX-stabilized MTs (48) reported half-times on the order of tens of minutes, consistent with the range estimated here. These kinetic estimates represent order-of-magnitude approximations derived from a simplified non-cooperative model and are applicable only to lattice states that do not undergo conformational adaptation during binding. Furthermore, they do not account for cooperative envelope formation or ligand-dependent lattice rearrangements observed in expanded microtubules. Nevertheless, the simulations demonstrate that the measured kinetics are compatible with the high-affinity tau binding and slow dissociation observed under the experimental conditions used.

Discussion

The discovery of taxanes introduced the possibility of blocking the cytomotive switch in the straight MT conformation (16). By stabilizing polymerized MTs, these compounds suppress controlled force generation during mitosis while preserving polymer mass. This led to the expectation that microtubule-stabilizing agents (MSAs) would cause less neurotoxicity than depolymerizing agents. However, clinical experience revealed that PTX and related taxane-site ligands induce substantial and often persistent neurotoxicity (18, 19), indicating that stabilization itself is not structurally neutral.

Our results (**Figures 1 and 2**) show that MSA-induced stabilization is accompanied by defined lattice remodeling. Rather than creating entirely new architectures, ligands selectively stabilize pre-existing compact (~4.06 nm) and expanded (~4.17 nm) longitudinal lattice states. Importantly, lattice expansion is not intrinsically linked to taxane-site occupancy or to stabilization per se. Some taxane-site ligands (e.g., DDM and ZMP) maintain compact lattices, whereas even a weakly stabilizing precursor such as BIII induces expansion. Moreover, small chemical modifications of PTX, such as C-7 substitution, can switch the preferred lattice state. These findings demonstrate that ligand chemistry, rather than binding site alone, determines longitudinal lattice bias.

Although longitudinal spacing exhibits quasi-binary behavior, lateral organization spans a broader structural landscape reflected in shifts of mean radius. Expanded lattices are generally associated with modest changes in mean radius, whereas compact-stabilizing ligands often produce larger lateral adjustments. However, longitudinal and lateral parameters are partially decoupled: combinations of drugs and nucleotide analogs generate lattices with similar axial spacing but different mean radii. Thus, stabilization and lattice geometry are separable properties.

Time-resolved experiments (**Figure 4**) further clarify the dynamics of these transitions. Longitudinal expansion or compaction occurs within the temporal resolution of the assay, whereas lateral equilibration proceeds more slowly. This asymmetry suggests that the compact and expanded states represent closely spaced conformational minima that can be rapidly interconverted, while redistribution of protofilament organization requires longer equilibration. Together with stoichiometry experiments (**Figure 3**) showing that partial occupancy is sufficient to shift lattice states, these findings support an ensemble-based model in which ligand binding biases a pre-existing conformational landscape rather than imposing a wholly new structure.

The functional consequences of lattice state selection are substantial (**Figure 7A**). Expanded lattices display reduced steady-state GTP hydrolysis, whereas compact lattices retain or enhance catalytic activity. Molecular simulations indicate that ligand binding subtly reshapes the conformational ensemble of the β1:α2 interdimer interface through helix H7, thereby modulating catalytic-site geometry at the E-site (**Figures S2 and S4**). These effects arise from coordinated, small-amplitude structural adjustments rather than large rearrangements, consistent with the high sensitivity of GTP hydrolysis to precise catalytic alignment (40).

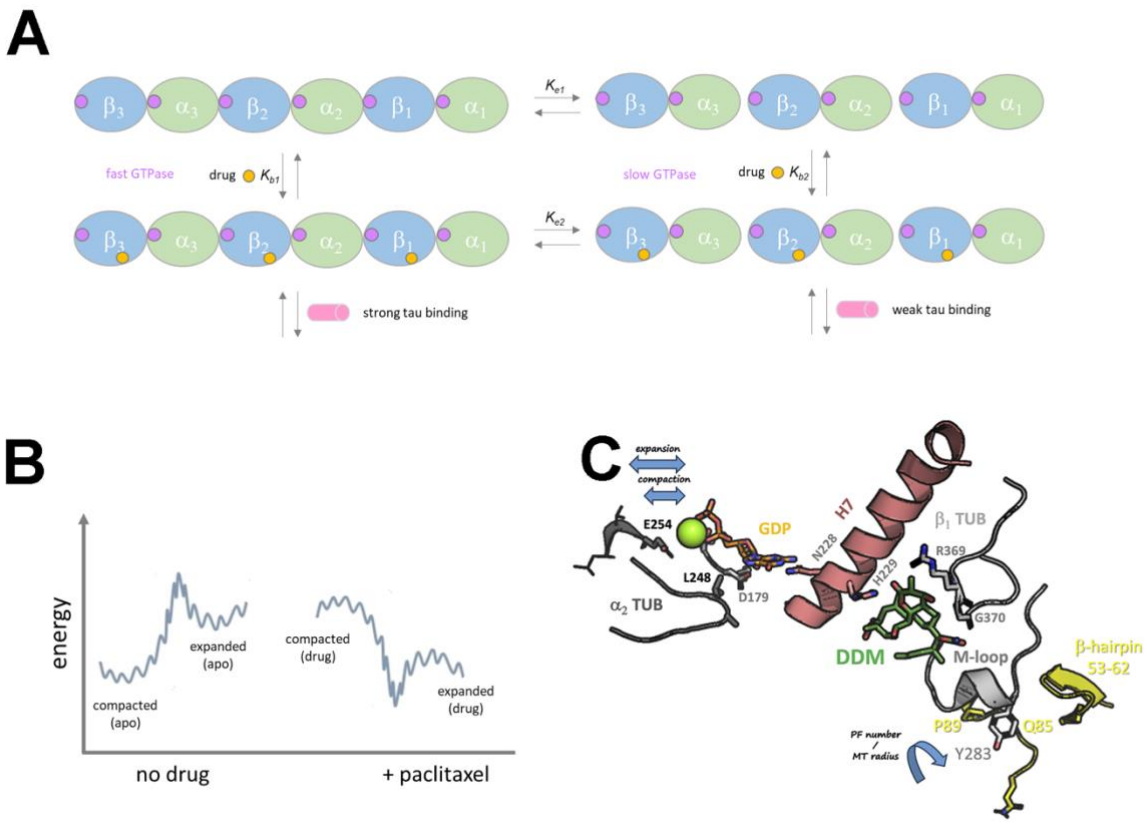

Figure 7 Conceptual model of ligand-induced lattice states and functional modulation. (A) Functional consequences of lattice state selection. Expanded lattices are associated with reduced GTP hydrolysis and weaker tau recognition, whereas compact lattices retain or enhance catalytic activity and promote stronger MAP interaction. The diagram integrates structural state selection with biochemical and regulatory outputs. **(B) Energy landscape of longitudinal lattice states** Schematic free-energy profile illustrating compact (~4.06 nm monomer rise) and expanded (~4.17 nm) lattice conformations as neighboring minima. Ligand binding shifts the population distribution between these states, consistent with the quasi-discrete axial spacings observed experimentally. **(C) Structural coupling between the taxane site and the catalytic E-site.** Simplified cartoon representation depicting the structural basis for the crosstalk at the β1:α2 interdimer interface from the luminal taxane-binding pocket to the E-site through helix H7 of β1-tubulin. Differences in interdimer rise distance and rearrangement of the 178-SDT-180 motif remodel γ-phosphate positioning and water organization around the Mg^{2+} ion (green sphere) for the water-mediated GTP hydrolysis catalyzed by E254 from α2-tubulin. The interprotofilament crosstalk is dominated by the lodging of Y273 into a cavity present in the β1 subunit of the neighboring protofilament (yellow). β1, light grey; α2, dark grey; DDM and GDP are shown as sticks with C atoms colored in green and orange, respectively. The green sphere is the Mg^{2+} ion. ModelArchive DOI: **10.5452/ma-ir5i7**

Beyond catalysis, lattice state influences MAP recognition and motor behavior. Kinesin velocity is consistently higher on expanded lattices, whereas compressed lattices exhibit more heterogeneous stepping dynamics. Strongly stabilizing ligands tend to restrict motor flexibility, whereas lower-affinity stabilizers permit faster progression. Tau, in contrast, shows a marked preference for compact lattices, binding rapidly and uniformly to some compressed states while interacting more slowly with expanded ones. Notably, tau recognition depends primarily on

longitudinal lattice state rather than mean radius alone, reinforcing the central role of axial conformation.

These observations converge in a unified model (**Figure 7**). Compact and expanded lattice states can be conceptualized as neighboring minima along a shared structural landscape (**Figure 7B**). Ligand binding shifts the population distribution between these states without generating entirely new geometries. Structural coupling between the luminal taxane pocket and the interdimer interface provides a pathway through which small chemical perturbations propagate to catalytic and regulatory interfaces (**Figure 7C**). In this framework, lattice conformation encodes for functional outputs, linking drug chemistry to enzymatic activity and MAP recognition.

Importantly, structural transitions occur at substoichiometric occupancy and longitudinal states interconvert within seconds, illustrating that modest chemical perturbations are sufficient to bias the conformational ensemble of the polymer. This sensitivity underscores the intrinsic plasticity of tubulin and supports a model in which compact and expanded states are separated by a small energetic difference that can be rapidly shifted by ligand binding. Therefore, MSAs act not only as stabilizers, but as modulators of lattice state.

Here, we have provided a quantitative structural atlas of ligand-induced lattice states and demonstrate that longitudinal conformation functions as a regulatory parameter linking chemical binding to catalytic and MAP-dependent outputs. By showing that ligand chemistry selectively biases rapidly interconvertible lattice states with distinct functional consequences, this work establishes the microtubule lattice as a tunable structural platform and offers a conceptual framework for the rational design of structure-selective modulators with improved therapeutic profiles.

Summary

Binding of stabilizing drugs to microtubules alters their structure both longitudinally and laterally. Along the longitudinal axis, the lattice adopts two preferred conformational states: a compact state (monomer rise ~4.06 nm) and an expanded state (~4.17 nm). These states are closely spaced energetically, as even partial ligand occupancy is sufficient to shift the conformational equilibrium, and longitudinal expansion or compaction occurs within seconds of drug incorporation.

In contrast, lateral organization spans a broader structural landscape reflected in shifts in mean microtubule radius. These variations correspond to differences in average protofilament organization within heterogeneous populations rather than discrete, synchronous protofilament transitions. Although alternative lateral arrangements appear energetically similar, allowing ligand binding to bias their distribution, equilibration toward the final mean radius occurs more gradually than longitudinal changes.

The conformational effects of these compounds can be finely tuned through subtle chemical modifications, such as acylation of the C-7 hydroxyl of PTX. These structural alterations are accompanied by changes in microtubule biochemical properties, including GTPase activity,

588 and significantly influence recognition by tau and kinesin. Together, these findings highlight
589 microtubule architecture as a tunable structural platform that integrates chemical perturbation with
590 catalytic and regulatory outputs.
591
592 **Materials and Methods**
593 ***Proteins and chemicals.***
594 Purified calf brain tubulin containing a mixture of isotypes (50) was prepared as described
595 (51) and used for biochemical and fiber diffraction experiments. Tau-mCherry was expressed and
596 purified as described previously (42). Human Kif5B–eGFP (amino acids 1–905), containing a C-
597 terminal fluorescent tag followed by a 3C protease cleavage site and a 6×His tag, was expressed
598 and purified as described in (52) with minor modifications. Prior to purification, cells were
599 resuspended in an equal volume of lysis buffer (30 mM HEPES pH 7.5, 300 mM NaCl, 0.5 mM
600 ATP, 5% glycerol, 20 mM imidazole, 0.5 mM Tris(2-carboxyethyl)phosphine (TCEP))
601 supplemented with 1× protease inhibitor cocktail and benzonase (25 U/mL). Cells were lysed,
602 and the lysate was clarified by centrifugation for 45 min at 40,000 rpm in a 45 Ti fixed-angle rotor
603 (Beckman Coulter) at 4 °C. The supernatant was incubated with pre-equilibrated HisPur™ Ni-
604 NTA agarose resin (Thermo Fisher Scientific) for 1 h at 4 °C with gentle rotation in a gravity-flow
605 column. The resin was washed with lysis buffer and subsequently with buffer B (30 mM HEPES
606 pH 7.5, 300 mM NaCl, 0.5 mM ATP, 5% glycerol, 30 mM imidazole, 0.5 mM TCEP). The protein
607 was eluted after overnight cleavage of the His tag with HRV 3C protease in lysis buffer at 4 °C.
608 The eluate was further purified by size-exclusion chromatography on a Superdex® 200 10/300
609 GL column equilibrated in exclusion buffer (30 mM HEPES pH 7.5, 300 mM NaCl, 0.5 mM ATP,
610 5% glycerol, 0.5 mM TCEP). Peak fractions were analyzed by SDS-PAGE, pooled, concentrated
611 using Amicon Ultra-15 centrifugal filter units (Millipore), aliquoted, snap-frozen in liquid nitrogen,
612 and stored at −80 °C.
613 GTP and GMPCPP were purchased from Jena Biosciences (Jena, Germany). Sodium
614 molybdate and malachite green oxalate were from Sigma-Aldrich. PTX was from Alfa Aesar; DTX
615 was kindly provided by Rhône-Poulenc Rorer (Aventis, Schiltigheim, France); CBTX and BIII were
616 from Sigma; Epo A, B, and D, TACCA-AJ, and IBP were from MedChemExpress; LAU and PLA
617 were provided by Victoria University of Wellington. CTX40, 101, and 102; 2-AB-PT; 3′N-AB-PT;
618 FTX-1; FTX-2; FCH-3; Azido-BIII; HXFTX; ATX; DDM; ZMP; DCT; TB282; CSTR; and CW235
619 were synthesized as described (16, 53-65). FB44 and FB53 were synthesized as described (34).
620 GS305 was synthesized as described (10.26434/chemrxiv-2024-nwb48). The synthesis and
621 characterization of PPH are described in patent PCT/EP2014/075903.
622 All compounds were dissolved in DMSO to a final concentration of 20 mM, aliquoted, and
623 stored at −80 °C until use.
624
625 ***Microtubule shear-flow alignment and X-ray fiber diffraction experiments.***
626 Microtubules were assembled from purified bovine brain tubulin (100 μM) in PM buffer
627 (80 mM K-PIPES, 1 mM EGTA, 1 mM dithiothreitol, 0.2 mM Tris, 3 mM $MgCl_2$, pH 6.8) in the

628 presence of either 2 mM GTP or 0.5 mM GMPCPP. Where indicated, drugs were included during
629 polymerization at the specified concentrations (typically 200 μM for static experiments). Additional
630 nucleotide analog conditions included 2 mM GTP + 10 mM BeF_3^- and 2 mM GTP + 500 μM $AlCl_3$
631 + 2 mM KHF_2 (used as the fluoride source for AlF_4^- formation), as well as combinations thereof
632 in the presence or absence of 200 μM PTX.
633 Polymerized tubulin was quantified by ultracentrifugation as described previously (66).
634 Under the conditions used, polymer levels ranged from ~85 μM in the absence of drug to ~99 μM
635 in the presence of GMPCPP and DDM. Drug occupancy was quantified by HPLC as described
636 (44). Stoichiometric ratios reported in **Figure 3** were corrected according to measured
637 polymerized tubulin and bound drug concentrations.
638 Static X-ray fiber diffraction data were collected at the BL11-NDC-SWEET beamline of
639 the ALBA Synchrotron (Cerdanyola del Vallès, Spain) at λ = 0.827 nm as described in (26).
640 Diffraction data were processed using our in-house software FiDAT (Fernández et al., manuscript
641 in preparation). Longitudinal lattice spacing (monomer rise) was determined directly from the
642 position of meridional layer lines corresponding to the fourth harmonic of the 4 nm axial repeat,
643 as described (20, 26). This axial parameter is obtained directly from peak positions and does not
644 rely on geometric modeling. Radial structural parameters (mean microtubule radius) were
645 determined from the position of the J_{02} equatorial maximum according to $J_{02} = 1.045/R$ nm^{-1}(where
646 R is the mean radius in nm). Protofilament number values reported in **Table I** and **Table SI** are
647 model-derived estimates calculated from the mean radius assuming an average inter-
648 protofilament spacing of 5.7 nm (27) and are provided for comparative purposes only. Errors
649 correspond to the standard error of the mean radius and monomer rise derived from peak-position
650 fitting.
651 Time-resolved X-ray fiber diffraction experiments were performed at the BL40XU
652 beamline of SPring-8 (Hyogo, Japan). A 100 μL aliquot of assembled MTs (100 μM tubulin) was
653 applied to the shear-flow alignment apparatus. At t = 40 s, 1 μL of a 20 mM DMSO stock solution
654 of stabilizing ligand (PTX, DTX, BIII, or LAU) was added by remote-controlled pipette to achieve
655 a final concentration of 200 μM (final DMSO concentration 1% v/v; matched DMSO controls were
656 performed). Diffraction patterns were recorded with a 0.8 m camera length and 0.95 s exposure
657 using a Pilatus 200K detector (Rigaku, Tokyo, Japan). Radial integration and peak extraction were
658 performed using ImageJ (v1.53c, NIH). Spatial calibration was performed using the 4.97 nm
659 powder diffraction signal of lead stearate. One detector pixel corresponded to a reciprocal-space
660 interval of 0.0011 nm^{-1}. Peak positions were determined by Lorentzian fitting of the diffraction
661 profiles.
662
663 ***In silico model building and molecular dynamics simulations.***
664 Geometry optimization and derivation of atom-centered RESP charges (67) for DTX, Epo
665 A, ZMP, DDM, and ATX were performed at the B3LYP/6-31G(d,p) level of theory using the IEF-
666 SCRF continuum solvent model (68) for water, as implemented in Gaussian 09 (Revision D.01)
667 (69). This protocol has been applied previously to other tubulin ligands (70) and to covalent

668 adducts of TACCA-AJ and ZMP with Aspβ226 and Hisβ229, respectively (37). Bonded and non-
669 bonded parameters were assigned using the general AMBER force field (GAFF2) (71).
670 The conformational preferences of DDM in explicit solvent were examined by immersing
671 the ligand (coordinates from PDB entry 6SES) in a cubic box of TIP3P water molecules and
672 simulating at 300 K for 300 ns using molecular dynamics (MD), followed by simulated annealing
673 and energy minimization, as described previously (34, 72).
674 Macromolecular models representing three parallel short protofilaments (PFs), each
675 consisting of two head-to-tail αβ dimers ((α1:β1–α2:β2)/(α1′:β1′–α2′:β2′)/(α1″:β1″–α2″:β2″)) (MT
676 patches), were constructed from PDB entries 6DPU and 6DPV (73) (expanded and compacted
677 14-PF MTs, respectively) and 3JAK (74) (symmetrized compact 13-PF MT). Missing residues 38–
678 46 in each α subunit were grafted from the AlphaFold model AF-P81947-F1-v4. Residue
679 numbering and secondary structure assignments follow α-tubulin conventions (75).
680 Refined 6DPV and 3JAK MT patches were subjected to anisotropic elastic network
681 modeling (ENM) and normal mode analysis (NMA) using the elNémo server (76) with default
682 parameters (12 Å cutoff; 1.0 kcal mol^{-1} $Å^{-2}$ force constant; maximum displacement <2 Å) (77).
683 The interdimer interface (β1:α2) was further examined using reduced complexes derived
684 from 6DPU (expanded) and 6DPV (compacted). All Cα atoms, except those in flexible loop
685 regions, were restrained using a weak harmonic force constant (2.0 kcal mol^{-1} $Å^{-2}$) to preserve
686 global lattice geometry. GTP at the N-site and either GTP or GDP at the β-tubulin E-site, including
687 partially hydrated Mg^{2+} ions, were positioned according to high-resolution structures (PDB 4I4T
688 and 8BDE). Systems were energy minimized and equilibrated at 300 K for 100 ps using the ff14SB
689 force field (78), GAFF2 for ligands, TIP3P water for explicitly retained water molecules, and the
690 generalized Born model for bulk solvent (79), as implemented in pmemd.cuda_SPFP of AMBER
691 18. These short simulations were intended for structural relaxation rather than production
692 sampling. Simulated annealing from 300 K to 100 K over 150 ps was subsequently applied.
693 The different (α1:β1–α2:β2)/(α1′:β1′–α2′:β2′)/(α1″:β1″–α2″:β2″) complexes in apo and
694 holo states were simulated under identical conditions for 200 ps to ensure local equilibration.
695 Ligands were positioned based on experimental binding modes: ATX and DTX were
696 superimposed onto PTX-bound structures (16); DDM and Epo B were docked to reproduce poses
697 observed in PDB entries 6SES and 7DAE; covalent adducts of TACCA-AJ and ZMP were
698 constructed as described (37). Six replicates of each ligand-bound system were sampled in
699 parallel.
700 The equilibrated MT patches were cooled from 300 K to 100 K over 400 ps and energy
701 minimized without positional restraints. Tubular assemblies were constructed by iterative best-fit
702 superposition of MT patches in PyMOL, following the procedure described in (34). The (α1:β1–
703 α2:β2–α3:β3) stretch of the first copy was superimposed onto the corresponding stretch of the
704 optimized model, and successive copies were iteratively aligned to generate 13- or 14-PF straight
705 microtubule segments (**Figure S5**) with one ligand bound per β subunit. Redundant overlapping
706 coordinates were removed, and the final all-atom models were energy refined and renumbered.

707 Twelve- and fifteen-PF assemblies were generated by superimposing PF segments onto the
708 harmonically deformed geometries obtained from NMA (**Supp. Movie 11**).
709 Representative models of one complete MT turn with bound PTX, DTX, Epo B, DDM,
710 ZMP, and TACCA-AJ have been deposited in the ModelArchive (www.modelarchive.org) with
711 accession codes ma-rkctk, ma-x9q02, ma-2embb, ma-ir5i7, ma-qcuyh, and ma-qzvr1,
712 respectively. The model containing bound ATX can be inferred from the Flutax-2-bound model
713 (ma-ayvpr) (34). The first non-trivial normal mode calculated for the Cα trace of the refined PTX-
714 bound 12-PF MT illustrates the cooperative closing motion associated with seam sealing (**Supp.**
715 **Movie 11**).
716
717 ***Measurement of nucleotide hydrolysis.***

718 Nucleotide hydrolysis by MTs was measured in MEDTA buffer (100 mM potassium 2-(N-
719 morpholino)ethanesulfonic acid (K-MES), 1 mM EDTA, 3.4 M glycerol (~30% v/v), pH 6.7)
720 supplemented with 6 mM $MgCl_2$ and 1 mM GTP. Lyophilized tubulin (10 mg) was resuspended in
721 0.5 mL MEDTA buffer containing 0.1 mM GTP or 1 μM GMPCPP and no $MgCl_2$. The solution was
722 passed through a Sephadex G-25 column (30 × 0.9 cm) to remove trehalose and phosphate
723 present in the storage buffer. Aggregates were removed by centrifugation at 50,000 rpm for 10
724 min at 4 °C using a Beckman Optima MAX-XP ultracentrifuge equipped with a TLA 120.2 fixed-
725 angle rotor. Tubulin concentration was determined spectrophotometrically (Evolution 201, Thermo
726 Scientific) using 1 cm quartz cuvettes. Absorbance spectra (240–340 nm) were recorded after
727 1:20 dilution in NaPi-SDS buffer. Concentrations were calculated using $\varepsilon_{(275)}$ = 107,000 M^{-1} cm^{-1}.
728 After concentration determination, $MgCl_2$ (6 mM) and 0.9 mM GTP was added to achieve final
729 concentrations of 1 mM GTP.

730 Tubulin polymerization was induced by raising the temperature to 37 °C in the presence
731 or absence of the indicated compounds, the percentage of tubulin polymerized was measured by
732 centrifugation as described (66) ranging between 85% (Apo) and 96% (DDM). Drugs were
733 present throughout polymerization and steady-state hydrolysis measurements. Polymer
734 assembly was monitored at 355 nm using an Appliskan® plate reader (Thermo Scientific).
735 Phosphate production was quantified under steady-state assembly conditions using the malachite
736 green inorganic phosphate assay (80). At defined time points, 20 μL aliquots were withdrawn and
737 immediately quenched into 280 μL Milli-Q water containing 0.7 M HCl (present in the malachite
738 green reagent), which denatures the protein and releases all inorganic phosphate present at the
739 time of quenching. Subsequently, 300 μL of malachite green solution (0.2% sodium molybdate,
740 0.03% malachite green oxalate, 0.05% Triton X-100, 0.7 M HCl) was added, mixed thoroughly,
741 and incubated according to the manufacturer's protocol. Absorbance was measured at 650 nm,
742 and phosphate concentrations were determined using sodium phosphate standards.

743 Because reactions were quenched under strongly denaturing conditions, the assay
744 measures cumulative inorganic phosphate generated at the time of sampling rather than
745 phosphate release kinetics. As GTP hydrolysis occurs only in polymerized tubulin, measured

746 activity reflects lattice-associated catalysis under steady-state assembly conditions. Nucleotide
747 content in drug-stabilized assembled MTs was quantified by centrifugation and HPLC as
748 described previously (66).

749

750 ***In vitro tau and kinesin- drug stabilized microtubules binding assay.***

751 *In vitro* binding of Kif5B(1–905)-eGFP and tau441-mCherry to drug-stabilized
752 microtubules was measured by total internal reflection fluorescence (TIRF) microscopy as
753 described in (48), replacing PTX with the indicated compounds. TIRF microscopy was performed
754 on an inverted Nikon Ti2-E widefield microscope equipped with a motorized XY stage, Perfect
755 Focus System, Apo TIRF 60× oil objective (NA 1.49), and a PRIME BSY camera (Teledyne
756 Photometrics). Microtubules (MTs) were visualized by interference reflection microscopy (IRM),
757 and fluorescently labeled proteins were visualized sequentially using GFP and mCherry filter
758 cubes. The microscope was controlled using NIS-Elements software (Nikon). All experiments
759 were conducted at room temperature.

760 Flow chambers were assembled from silanized glass coverslips (22 × 22 mm and 18 ×
761 18 mm) separated by parafilm strips (heated 15–20 s at 60 °C and gently pressed together),
762 generating ~2.5 mm-wide flow channels. Coverslips were washed in 3 M KOH, plasma-cleaned
763 (Zepto Plasma Cleaner, Diener Electronic), and silanized with hexamethyldisilazane. Channels
764 were incubated with 40 µg mL^{-1} anti-biotin antibodies (Sigma, B3640) in PBS for 10 min, followed
765 by blocking with 1% Pluronic F127 (Sigma-Aldrich, P2443) in PBS for at least 1 h. Excess blocker
766 was removed with BRB80 buffer (80 mM PIPES, 1 mM EGTA, 1 mM $MgCl_2$, pH 6.9).

767 MTs were assembled from porcine brain tubulin purified using the high-molarity PIPES
768 procedure (81). Polymerization reactions contained 2% biotinylated tubulin (Cytoskeleton Inc.,
769 T333P). Drug-stabilized MTs were polymerized from 4 mg mL^{-1} tubulin for 30 min at 37 °C in
770 BRB80 supplemented with 4 mM $MgCl_2$, 1 mM GTP, 40 µM of the indicated drug, and 5% DMSO.
771 MTs were pelleted for 30 min at 18,000 × g (Microfuge 18, Beckman Coulter), resuspended, and
772 stored in BRB80 containing 10 µM drug. All drug-stabilized MTs were stored and imaged in the
773 continuous presence of the corresponding ligand. GMPCPP-stabilized MTs were assembled from
774 4 mg mL^{-1} tubulin for 2 h at 37 °C in BRB80 supplemented with 1 mM $MgCl_2$ and 1 mM GMPCPP.
775 MTs were pelleted at 18,000 × g for 30 min and resuspended in BRB80.

776 Stabilized MTs were introduced into the flow channel and allowed to attach for around
777 10 s. Unbound MTs were removed by washing with BRB80 containing 10 µM of the corresponding
778 drug. Prior to imaging, buffer was exchanged to motility buffer (BRB80 containing 10 mM DTT,
779 20 mM D-glucose, 0.1% Tween 20, 0.5 mg mL^{-1} casein, 1 mM Mg-ATP, 0.02 mg mL^{-1} catalase,
780 0.22 mg mL^{-1} glucose oxidase, and 10 µM drug). Subsequently, either 1.08 nM Kif5B(1–905)-
781 eGFP or 5/10 nM tau441-mCherry in motility buffer was introduced into the chamber.

782 For kinesin motility assays, an IRM image (50 ms exposure) was acquired, followed by a
783 1 min video under 488 nm excitation (20% laser power, 300 ms exposure) with no delay. Three
784 to four videos were recorded from different fields within the same channel, with at least two

785 channels analyzed per condition. Experiments were repeated on 2–3 independent days, yielding
786 a total of 36-48 analyzed MTs per replicate.
787 For tau binding assays, 4 min videos were acquired at 7 s intervals. IRM (50 ms exposure)
788 and 561 nm fluorescence (30% laser power, 200 ms exposure) were recorded sequentially.
789 Depending on the drug used, firstly 5/10 nM tau-mCherry was injected immediately after the first
790 frame was acquired. Similarly, a second/third video of the same area was recorded adding up to
791 10/40 (second video) and 40 nM (if third video) tau-mCherry.
792 Because MTs were immobilized on a surface and non-immobilized ones washed
793 afterward, the effective concentration of accessible binding sites cannot be precisely defined,
794 Nevertheless, we can place an upper bound on the effective concentration of binding sites. Since
795 the chamber volume is approximately 8 µL, and in the tau experiments this protein is introduced
796 by flowing ~20 µL of a 5 nM solution and ZMP- stabilized MTs reach saturation under these
797 conditions and do not exhibit increased binding upon further increases in tau concentration, the
798 total accessible binding site concentration must be in the low-nM range, with an upper bound of
799 approximately 12.5 nM. Tau binding kinetics were qualitatively analyzed using a simple single-
800 step binding simulation (https://www.stolaf.edu/depts/chemistry/courses/toolkits/126/js/kinetics/)
801 using initial concentrations in the low nM range (**Supp. Figure 3** 12.5 nM binding sites and 5 nM
802 tau). These simulations reproduce both the observed timescale and saturation behavior.
803
804 ***Image analysis***.
805 For representative figures, data were collected from at least two independent
806 experimental replicates. Unless otherwise stated, image analysis was performed manually using
807 Fiji (ImageJ) (82). Graphs and statistical analyses were generated using GraphPad Prism v8.0.1.
808 Data are presented as mean ± standard error of the mean (SEM), unless otherwise specified.
809 Background fluorescence was subtracted from all intensity measurements prior to
810 analysis. For each condition, 12 MTs per channel were randomly selected among well-separated,
811 in-focus filaments identified in the IRM channel. Selection was performed prior to fluorescence
812 quantification to avoid bias. MTs exhibiting overlaps, obvious defects, or drifting during acquisition
813 were excluded from analysis.
814 For kinesin motility measurements, MTs were traced in the IRM channel using segmented
815 lines 5 pixels wide. Kymographs were generated using the *KymographBuilder* plugin in Fiji.
816 Individual motor trajectories were manually traced as 1-pixel-wide straight lines on the
817 kymographs. From these traces: Run length was determined from the displacement along the x-
818 axis. Run duration (dwell time) was determined from the y-axis. Velocity was calculated as run
819 length divided by run duration. Landing rate was calculated by counting the total number of motor
820 binding events per MT and normalizing to both the MT length (µm) and acquisition time (s), and
821 is reported as events·$\mu m^{-1} \cdot s^{-1}$. For each condition, analyses included MTs from at least two
822 independent experiments performed on different days.
823 To quantify the fraction of MT surface covered by tau envelopes, segmented lines (5
824 pixels wide; corresponding to 0.36 µm under our imaging conditions) were manually drawn along

envelope-covered regions or along the full MT length. The total envelope length was divided by the total MT length to yield the percentage of coverage. Coverage analysis was performed at defined time points: 12 s, 1 min, 2 min, and 4 min for the first acquisition (5 or 10 nM tau), and 12 s, 2 min, and 4 min for subsequent tau concentrations. To quantify tau binding per unit length, segmented lines (5 pixels wide) were drawn along the full MT length. The integrated fluorescence density (Relative I) was measured, background-subtracted, and normalized to MT length (µm), yielding fluorescence intensity per µm. All analyses were performed on at least two independent experiments per condition (24 MTs per replica).

Disclosure of delegation to Generative AI

The authors declare the use of generative AI in the writing process. The following tasks were delegated to GAI tools under full human supervision: Proofreading and editing, summarizing text. The GAI tool used was: Chat-GPT 5.4. Responsibility for the final manuscript lies entirely with the authors. GAI tools are not listed as authors and do not bear responsibility for the final outcomes.

Acknowledgements.

This work was supported by the Ministerio de Ciencia e Innovación (MICIN) and FEDER (PID2022-136765OB-I00 to J.F.D. and PID2021-123399OB-I00 to M.A.O.), by the European Molecular Biology Organization (EMBO) through a Short-Term Fellowship (No. 11234 to R.P.O.), and by MOSBRI (TNA) under project number MOSBRI-2024-296 to R.P.O. We thank the staff of beamline BL11-NCD-SWEET at the ALBA Synchrotron (Cerdanyola del Vallès, Spain) for excellent technical support. Time-resolved kinetic experiments were performed with the approval of the SPring-8 Proposal Review Committee (proposal numbers 2016B1182, 2020A1332, and 2021A1430). We also gratefully acknowledge Ganadería Fernando Díaz for the supply of calf brains.

References.

1. I. Grigoriev, A. Akhmanova, Microtubule dynamics at the cell cortex probed by TIRF microscopy. *Methods Cell Biol* **97**, 91-109 (2010).
2. J. M. Wagstaff *et al.*, Diverse cytomotive actins and tubulins share a polymerization switch mechanism conferring robust dynamics. *Science Advances* **9**, eadf3021 (2023).
3. R. B. Ravelli *et al.*, Insight into Tubulin Regulation from a Complex with Colchicine and a Stathmin-like Domain. *Nature* **428**, 198-202 (2004).
4. R. M. Buey, J. F. Díaz, J. M. Andreu, The Nucleotide Switch of Tubulin and Microtubule Assembly: a Polymerization-driven Structural Change. *Biochemistry* **45**, 5933-5938 (2006).
5. L. M. Rice, E. A. Montabana, D. A. Agard, The lattice as allosteric effector: structural studies of alphabeta- and gamma-tubulin clarify the role of GTP in microtubule assembly. *Proc Natl Acad Sci U S A* **105**, 5378-5383 (2008).
6. S. Y. Saito, Toxins affecting actin filaments and microtubules. *Prog Mol Subcell Biol* **46**, 187-219 (2009).
7. M. O. Steinmetz, A. E. Prota, Microtubule-Targeting Agents: Strategies To Hijack the Cytoskeleton. *Trends Cell Biol* **28**, 776-792 (2018).

8. S. Matthew *et al.*, Gatorbulin-1, a distinct cyclodepsipeptide chemotype, targets a seventh tubulin pharmacological site. *Proceedings of the National Academy of Sciences* **118**, e2021847118 (2021).
9. T. Mühlethaler *et al.*, Rational Design of a Novel Tubulin Inhibitor with a Unique Mechanism of Action. *Angew Chem Int Ed Engl* **61**, e202204052 (2022).
10. B. Gigant *et al.*, Structural basis for the regulation of tubulin by vinblastine. *Nature* **435**, 519-522 (2005).
11. A. E. Prota *et al.*, A new tubulin-binding site and pharmacophore for microtubule-destabilizing anticancer drugs. *Proc Natl Acad Sci U S A* **111**, 13817-13821 (2014).
12. A. E. Prota *et al.*, Pironetin Binds Covalently to alphaCys316 and Perturbs a Major Loop and Helix of alpha-Tubulin to Inhibit Microtubule Formation. *J Mol Biol* **428**, 2981-2988 (2016).
13. J. Yang *et al.*, Pironetin reacts covalently with cysteine-316 of alpha-tubulin to destabilize microtubule. *Nat Commun* **7**, 12103 (2016).
14. G.-z. Li *et al.*, Vincristine-induced peripheral neuropathy: A mini-review. *NeuroToxicology* **81**, 161-171 (2020).
15. R. C. Donehower, The Clinical Development of Paclitaxel: A Successful Collaboration of Academia, Industry and the National Cancer Institute. *The Oncologist* **1**, 240-243 (1996).
16. A. E. Prota *et al.*, Structural insight into the stabilization of microtubules by taxanes. *eLife* **12**, e84791 (2023).
17. A. E. Prota *et al.*, Structural basis of microtubule stabilization by laulimalide and peloruside A. *Angew Chem Int Ed Engl* **53**, 1621-1625 (2014).
18. B. M. Cook *et al.*, Differential Morphological and Biochemical Recovery from Chemotherapy-Induced Peripheral Neuropathy Following Paclitaxel, Ixabepilone, or Eribulin Treatment in Mouse Sciatic Nerves. *Neurotox Res* **34**, 677-692 (2018).
19. C. Pellacani, G. Eleftheriou, Neurotoxicity of antineoplastic drugs: Mechanisms, susceptibility, and neuroprotective strategies. *Advances in Medical Sciences* **65**, 265-285 (2020).
20. J. Estévez-Gallego *et al.*, Chemical modulation of microtubule structure through the laulimalide/peloruside site. *Structure* **31**, 88-99.e85 (2023).
21. A. Akhmanova, M. O. Steinmetz, Microtubule +TIPs at a glance. *J Cell Sci* **123**, 3415-3419 (2010).
22. D. R. Peet, N. J. Burroughs, R. A. Cross, Kinesin expands and stabilizes the GDP-microtubule lattice. *Nature Nanotechnology* **13**, 386-391 (2018).
23. V. Siahaan *et al.*, Microtubule lattice spacing governs cohesive envelope formation of tau family proteins. *Nat Chem Biol* **18**, 1224-1235 (2022).
24. E. Gornstein, T. L. Schwarz, The paradox of paclitaxel neurotoxicity: Mechanisms and unanswered questions. *Neuropharmacology* **76 Pt A**, 175-183 (2014).
25. J. M. Andreu *et al.*, Low resolution structure of microtubules in solution. Synchrotron X-ray scattering and electron microscopy of taxol-induced microtubules assembled from purified tubulin in comparison with glycerol and MAP-induced microtubules. *J Mol Biol* **226**, 169-184 (1992).
26. J. Estevez-Gallego *et al.*, Structural model for differential cap maturation at growing microtubule ends. *Elife* **9** (2020).
27. J. M. Andreu *et al.*, Solution structure of Taxotere-induced microtubules to 3-nm resolution. The change in protofilament number is linked to the binding of the taxol side chain. *J Biol Chem* **269**, 31785-31792 (1994).
28. R. Matesanz *et al.*, Modulation of microtubule interprotofilament interactions by modified taxanes. *Biophys J* **101**, 2970-2980 (2011).
29. M. R. Mejillano, J. S. Barton, J. P. Nath, R. H. Himes, GTP analogues interact with the tubulin exchangeable site during assembly and upon binding. *Biochemistry* **29**, 1208-1216 (1990).
30. A. A. Hyman, D. Chrétien, I. Arnal, R. H. Wade, Structural changes accompanying GTP hydrolysis in microtubules: information from a slowly hydrolyzable analogue guanylyl-(alpha,beta)-methylene-diphosphonate. *Journal of Cell Biology* **128**, 117-125 (1995).
31. Gregory M. Alushin *et al.*, High-Resolution Microtubule Structures Reveal the Structural Transitions in αβ-Tubulin upon GTP Hydrolysis. *Cell* **157**, 1117-1129 (2014).
32. B. J. LaFrance *et al.*, Structural transitions in the GTP cap visualized by cryo-electron microscopy of catalytically inactive microtubules. *Proceedings of the National Academy of Sciences* **119**, e2114994119 (2022).

33. T. Sugiyama *et al.*, Quick shear-flow alignment of biological filaments for X-ray fiber diffraction facilitated by methylcellulose. *Biophys J* **97**, 3132-3138 (2009).
34. F. Bonato *et al.*, Probing the structural signaling of microtubules with engineered, chemically controlled filaments. *BioRxiv* https://doi.org/10.1101/2025.10.23.684077 (2025).
35. E. H. Kellogg *et al.*, Insights into the Distinct Mechanisms of Action of Taxane and Non-Taxane Microtubule Stabilizers from Cryo-EM Structures. *J Mol Biol* **429**, 633-646 (2017).
36. J. F. Díaz, J. M. Valpuesta, P. Chacón, G. Diakun, J. M. Andreu, Changes in microtubule protofilament number induced by Taxol binding to an easily accessible site. Internal microtubule dynamics. *J Biol Chem* **273**, 33803-33810 (1998).
37. P. A. Sánchez-Murcia, A. Mills, Á. Cortés-Cabrera, F. Gago, Unravelling the covalent binding of zampanolide and taccalonolide AJ to a minimalist representation of a human microtubule. *Journal of computer-aided molecular design* **33**, 627-644 (2019).
38. G. Tauriello *et al.*, ModelArchive: A Deposition Database for Computational Macromolecular Structural Models. *Journal of Molecular Biology* **437**, 168996 (2025).
39. E. Nogales, K. H. Downing, L. A. Amos, J. Lowe, Tubulin and FtsZ form a distinct family of GTPases. *Nat Struct Biol* **5**, 451-458 (1998).
40. B. Ram Prasad, N. V. Plotnikov, J. Lameira, A. Warshel, Quantitative exploration of the molecular origin of the activation of GTPase. *Proceedings of the National Academy of Sciences* **110**, 20509-20514 (2013).
41. K. J. Verhey, J. W. Hammond, Traffic control: regulation of kinesin motors. *Nature reviews. Molecular cell biology* **10**, 765-777 (2009).
42. M. Genova *et al.*, Tubulin polyglutamylation differentially regulates microtubule-interacting proteins. *Embo j* **42**, e112101 (2023).
43. R. M. Buey *et al.*, Interaction of Epothilone Analogs with the Paclitaxel Binding Site; Relationship between Binding Affinity, Microtubule Stabilization, and Cytotoxicity. *Chem Biol* **11**, 225-236 (2004).
44. R. M. Buey *et al.*, Microtubule Interactions with Chemically Diverse Stabilizing Agents: Thermodynamics of Binding to the Paclitaxel Site Predicts Cytotoxicity. *Chemistry & Biology* **12**, 1269-1279 (2005).
45. J. J. Field *et al.*, Zampanolide, a potent new microtubule-stabilizing agent, covalently reacts with the taxane luminal site in tubulin alpha,beta-heterodimers and microtubules. *Chem Biol* **19**, 686-698 (2012).
46. R. Brandt, N. I. Trushina, L. Bakota, Much More Than a Cytoskeletal Protein: Physiological and Pathological Functions of the Non-microtubule Binding Region of Tau. *Front Neurol* **11**, 590059 (2020).
47. R. Tan *et al.*, Microtubules gate tau condensation to spatially regulate microtubule functions. *Nat Cell Biol* **21**, 1078-1085 (2019).
48. V. Siahaan *et al.*, Kinetically distinct phases of tau on microtubules regulate kinesin motors and severing enzymes. *Nat Cell Biol* **21**, 1086-1092 (2019).
49. K. Johnson, *Kinetic analysis of macromolecules : a practical approach*, Practical approach series ; 267. (Oxford University Press, Oxford ;, 2003).
50. R. F. Ludueña, A. Banerjee, "The Isotypes of Tubulin" in The Role of Microtubules in Cell Biology, Neurobiology, and Oncology, T. Fojo, Ed. (Humana Press, Totowa, NJ, 2008), 10.1007/978-1-59745-336-3_6, pp. 123-175.
51. J. M. Andreu, "Large Scale Purification of Brain Tubulin With the Modified Weisenberg Procedure" in Microtubule Protocols, J. Zhou, Ed. (Humana Press, Totowa, NJ, 2007), 10.1007/978-1-59745-442-1_2, pp. 17-28.
52. V. Henrichs *et al.*, Mitochondria-adaptor TRAK1 promotes kinesin-1 driven transport in crowded environments. *Nature Communications* **11**, 3123 (2020).
53. A. A. Souto *et al.*, New fluorescent water-soluble taxol derivatives. *Angew Chem Int Ed Engl* **34**, 2710-2712 (1995).
54. Y. Li, R. Edsall, Jr., P. G. Jagtap, D. G. Kingston, S. Bane, Equilibrium studies of a fluorescent paclitaxel derivative binding to microtubules. *Biochemistry* **39**, 616-623 (2000).
55. Y. Han *et al.*, Interaction of a fluorescent derivative of paclitaxel (Taxol) with microtubules and tubulin-colchicine. *Biochemistry* **35**, 14173-14183 (1996).
56. L. He *et al.*, A common pharmacophore for Taxol and the epothilones based on the biological activity of a taxane molecule lacking a C-13 side chain. *Biochemistry* **39**, 3972-3978 (2000).

57. J. F. Diaz, R. Strobe, Y. Engelborghs, A. A. Souto, J. M. Andreu, Molecular recognition of taxol by microtubules. Kinetics and thermodynamics of binding of fluorescent taxol derivatives to an exposed site. *J Biol Chem* **275**, 26265-26276 (2000).
58. C. D. Vanderwal, D. A. Vosburg, S. Weiler, E. J. Sorensen, An enantioselective synthesis of FR182877 provides a chemical rationalization of its structure and affords multigram quantities of its direct precursor. *J Am Chem Soc* **125**, 5393-5407 (2003).
59. I. Paterson, I. Lyothier, Total synthesis of (+)-discodermolide: an improved endgame exploiting a Still-Gennari-type olefination with a C1-C8 beta-ketophosphonate fragment. *Org Lett* **6**, 4933-4936 (2004).
60. J. F. Diaz, I. Barasoain, A. A. Souto, F. Amat-Guerri, J. M. Andreu, Macromolecular accessibility of fluorescent taxoids bound at a paclitaxel binding site in the microtubule surface. *J Biol Chem* **280**, 3928-3937 (2005).
61. R. Matesanz *et al.*, Optimization of taxane binding to microtubules. Binding affinity decomposition and incremental construction of a high-affinity analogue of paclitaxel. *Chem Biol* **15**, 573-585 (2008).
62. X. Li, I. Barasoain, R. Matesanz, J. F. Diaz, W. S. Fang, Synthesis and biological activities of high affinity taxane-based fluorescent probes. *Bioorg Med Chem Lett* **19**, 751-754 (2009).
63. D. Zurwerra *et al.*, Total Synthesis of (−)-Zampanolide and Structure–Activity Relationship Studies on (−)-Dactylolide Derivatives. *Chemistry – A European Journal* **18**, 16868-16883 (2012).
64. C. W. Wullschleger, J. Gertsch, K.-H. Altmann, Synthesis and Biological Activity of 7,8,9-Trideoxy- and 7R DesTHP-Peloruside A. *Chemistry – A European Journal* **19**, 13105-13111 (2013).
65. T. M. Brütsch *et al.*, Synthesis and Structure-Activity Relationship Studies of C(13)-Desmethylene-(−)-Zampanolide Analogs. *Chemistry – A European Journal* **29**, e202300703 (2023).
66. J. F. Díaz, J. M. Andreu, Assembly of Purified GDP-Tubulin into Microtubules induced by Taxol and Taxotere: Reversibility, Ligand Stoichiometry, and Competition. *Biochemistry* **32**, 2747-2755 (1993).
67. J. Wang, P. Cieplak, P. A. Kollman, How well does a restrained electrostatic potential (RESP) model perform in calculating conformational energies of organic and biological molecules? *Journal of Computational Chemistry* **21**, 1049-1074 (2000).
68. G. Scalmani, M. J. Frisch, Continuous surface charge polarizable continuum models of solvation. I. General formalism. *J Chem Phys* **132**, 114110 (2010).
69. M. J. Frisch *et al.* (2009) Gaussian 09. (Gaussian, Inc., Wallingford, CT, USA).
70. Y. Ma *et al.*, Modulation of taxane binding to tubulin curved and straight conformations by systematic 3′N modification provides for improved microtubule binding, persistent cytotoxicity and in vivo potency. *European Journal of Medicinal Chemistry* **259**, 115668 (2023).
71. X. He, V. H. Man, W. Yang, T. S. Lee, J. Wang, A fast and high-quality charge model for the next generation general AMBER force field. *J Chem Phys* **153**, 114502 (2020).
72. C. Coderch *et al.*, A structure-based design of new C2- and C13-substituted taxanes: tubulin binding affinities and extended quantitative structure-activity relationships using comparative binding energy (COMBINE) analysis. *Org Biomol Chem* **11**, 3046-3056 (2013).
73. R. Zhang, B. LaFrance, E. Nogales, Separating the effects of nucleotide and EB binding on microtubule structure. *Proc. Natl. Acad. Sci. USA* **115**, E6191-E6200 (2018).
74. R. Zhang, G. M. Alushin, A. Brown, E. Nogales, Mechanistic Origin of Microtubule Dynamic Instability and Its Modulation by EB Proteins. *Cell* **162**, 849-859 (2015).
75. J. Löwe, H. Li, K. H. Downing, E. Nogales, Refined structure of alpha beta-tubulin at 3.5 A resolution. *J Mol Biol* **313**, 1045-1057 (2001).
76. K. Suhre, Y.-H. Sanejouand, ElNémo: a normal mode web server for protein movement analysis and the generation of templates for molecular replacement. *Nucleic acids research* **32**, W610-W614 (2004).
77. A. R. Atilgan *et al.*, Anisotropy of fluctuation dynamics of proteins with an elastic network model. *Biophys J* **80**, 505-515 (2001).
78. J. A. Maier *et al.*, ff14SB: Improving the Accuracy of Protein Side Chain and Backbone Parameters from ff99SB. *Journal of Chemical Theory and Computation* **11**, 3696-3713 (2015).

79. A. V. Onufriev, D. A. Case, Generalized Born Implicit Solvent Models for Biomolecules. *Annu Rev Biophys* **48**, 275-296 (2019).
80. S. G. Carter, D. W. Karl, Inorganic phosphate assay with malachite green: An improvement and evaluation. *Journal of Biochemical and Biophysical Methods* **7**, 7-13 (1982).
81. M. Castoldi, A. V. Popov, Purification of brain tubulin through two cycles of polymerization-depolymerization in a high-molarity buffer. *Protein Expr Purif* **32**, 83-88 (2003).
82. J. Schindelin *et al.*, Fiji: an open-source platform for biological-image analysis. *Nature Methods* **9**, 676-682 (2012).

TAXANES

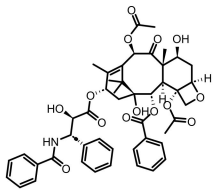

Paclitaxel (**PTX**)

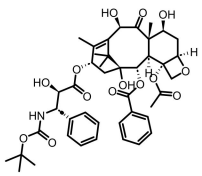

Docetaxel (**DTX**)

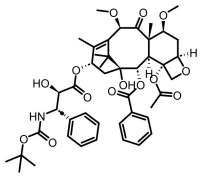

Cabazitaxel (**CBTX**)

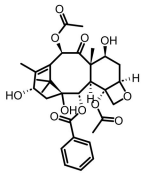

Baccatin III (**BIII**)

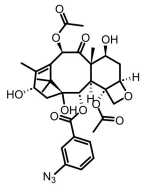

2m-azido baccatin III (**Azido-BIII**)

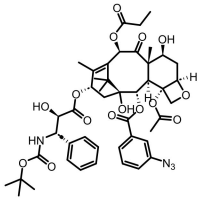

Chitax-40 (**CTX40**)

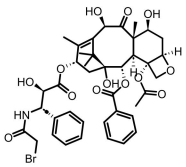

Chitax 101 (**CTX101**)

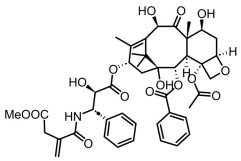

Chitax 102 (**CTX102**)

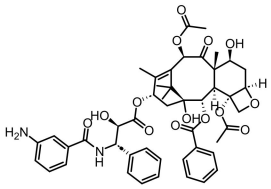

3´N-Aminobenzoyl paclitaxel (**3'N-PT**)

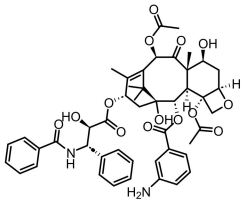

2-Aminobenzoyl paclitaxel (**2-AB-PT**)

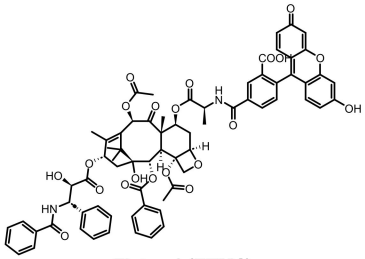

Flutax 1 (**FTX1**)

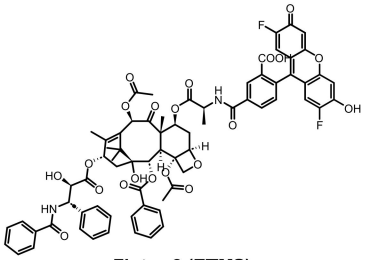

Flutax 2 (**FTX2**)

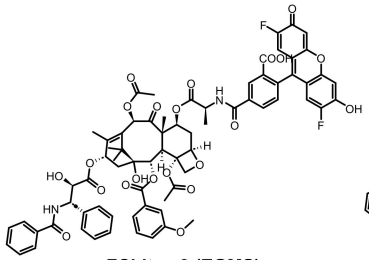

FChitax-3 (**FCH3**)

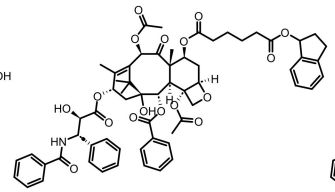

FB44

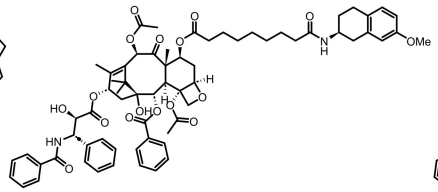

FB53

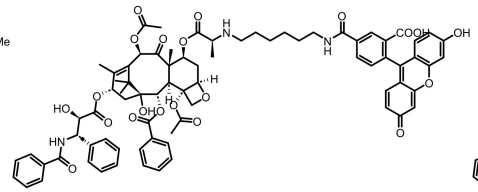

Hexaflutax (**HXFTX**)

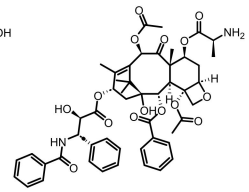

Alanylpaclitaxel (**ATX**)

EPOTHILONES

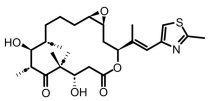

Epothilone A (**Epo A**)

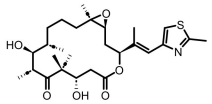

Epothilone B (**Epo B**)

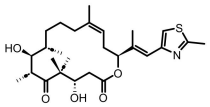

Epothilone D (**Epo D**)

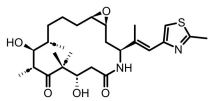

Ixabepilone (**IBP**)

ZAMPANOLIDES

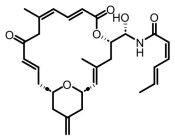

Zampanolide (**ZMP**)

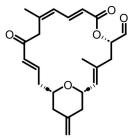

Dactylolide (**DCT**)

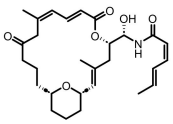

TB282

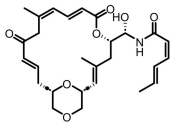

GS305

OTHER TAXANE SITE BINDERS

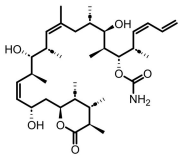

Discodermolide (**DDM**)

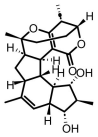

Cyclostreptin (**CSTR**)

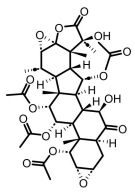

Taccalonolide AJ (**TACCA-AJ**)

LAULIMALIDE/PELORUSIDES

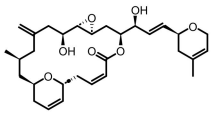

Laulimalide (**LAU**)

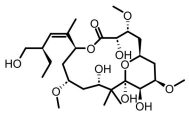

Peloruside (**PLA**)

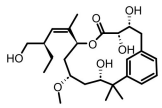

Pelophen B (**PPH**)

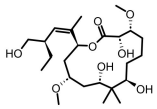

CW235

MT size vs lattice state

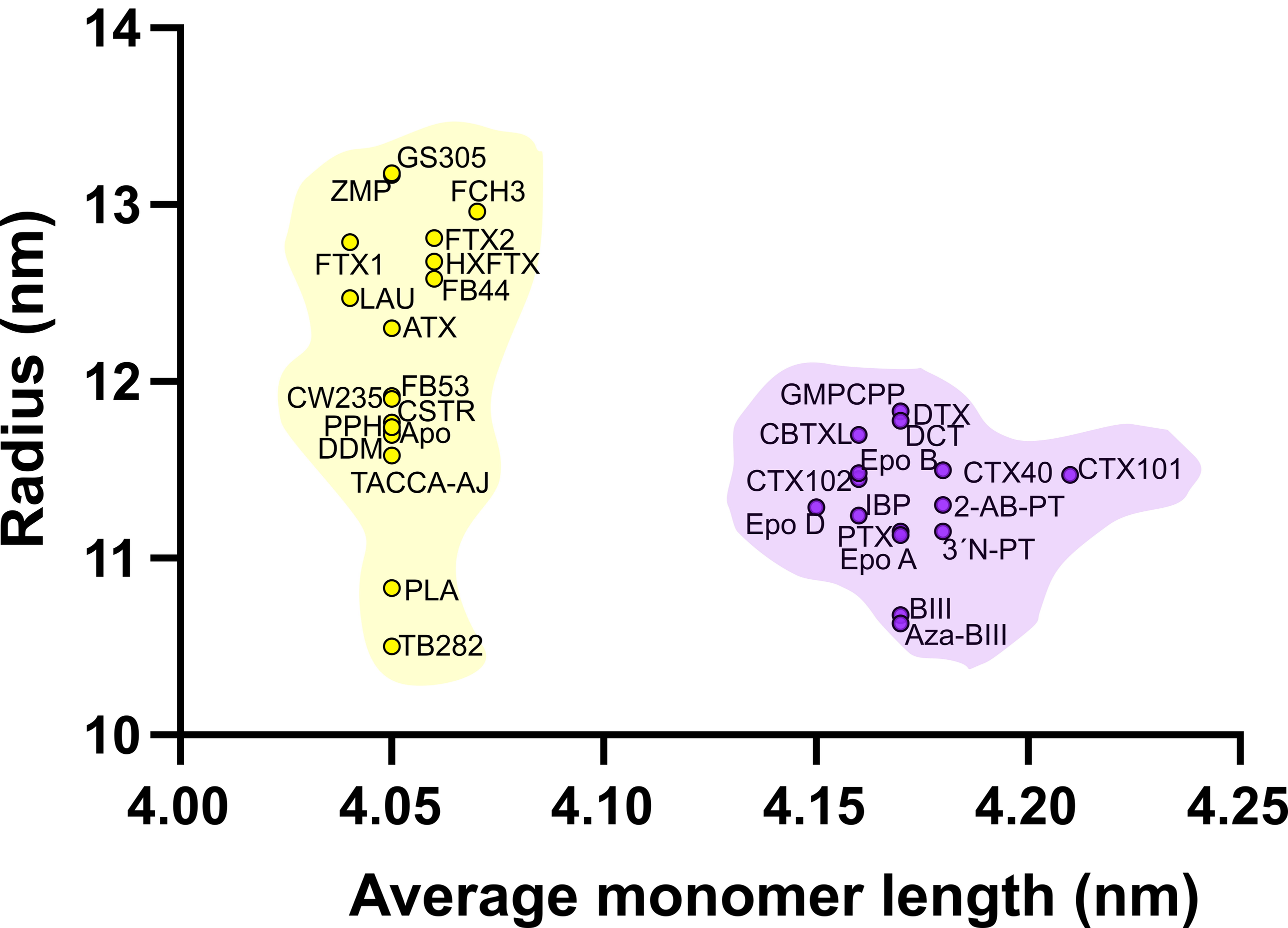

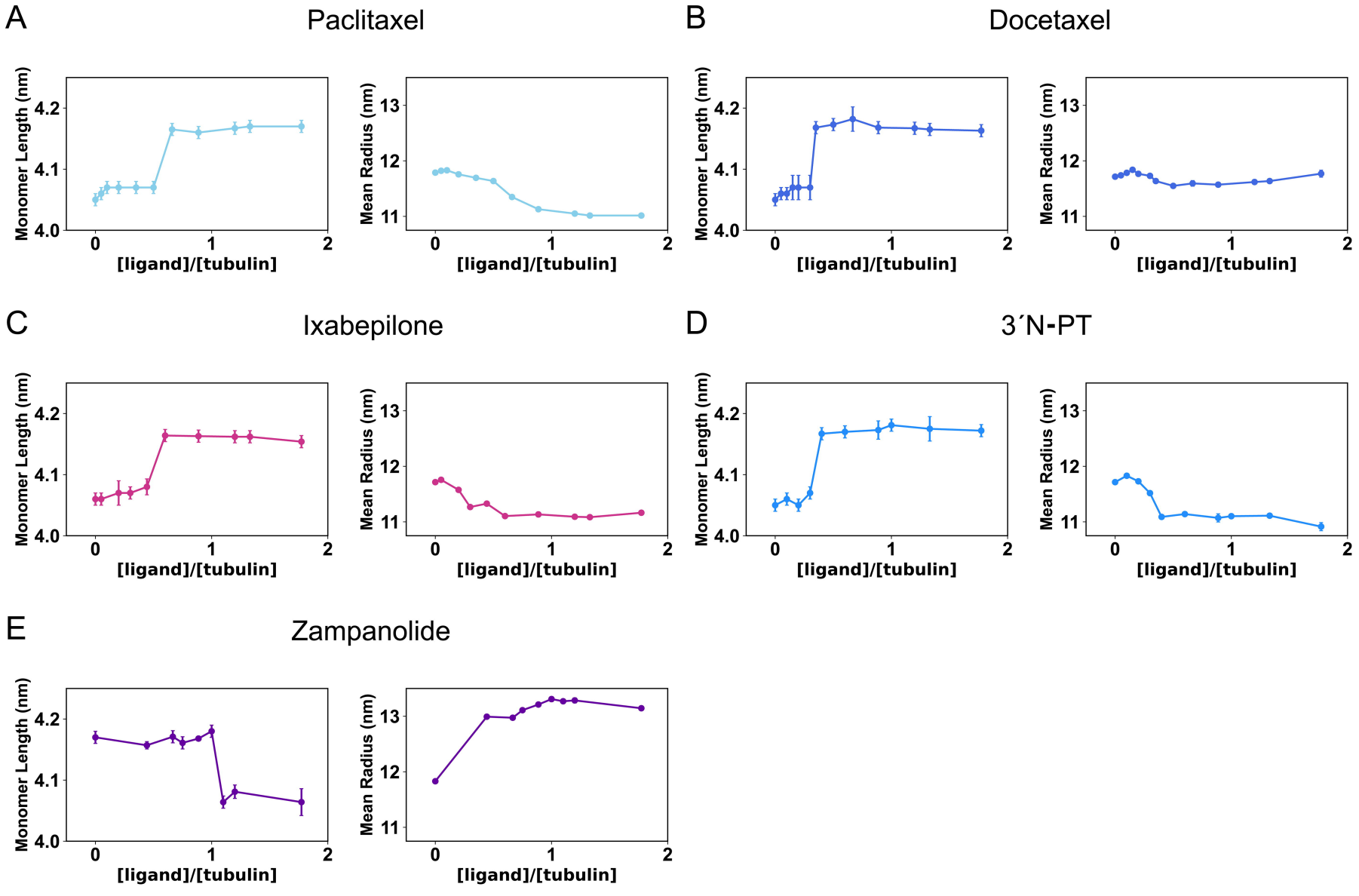
A
Paclitaxel
B
Docetaxel
C
Ixabepilone
D
3´N-PT
E
Zampanolide
Monomer Length (nm)
Mean Radius (nm)
[ligand]/[tubulin]
4.0
4.1
4.2
11
12
13
0
1
2

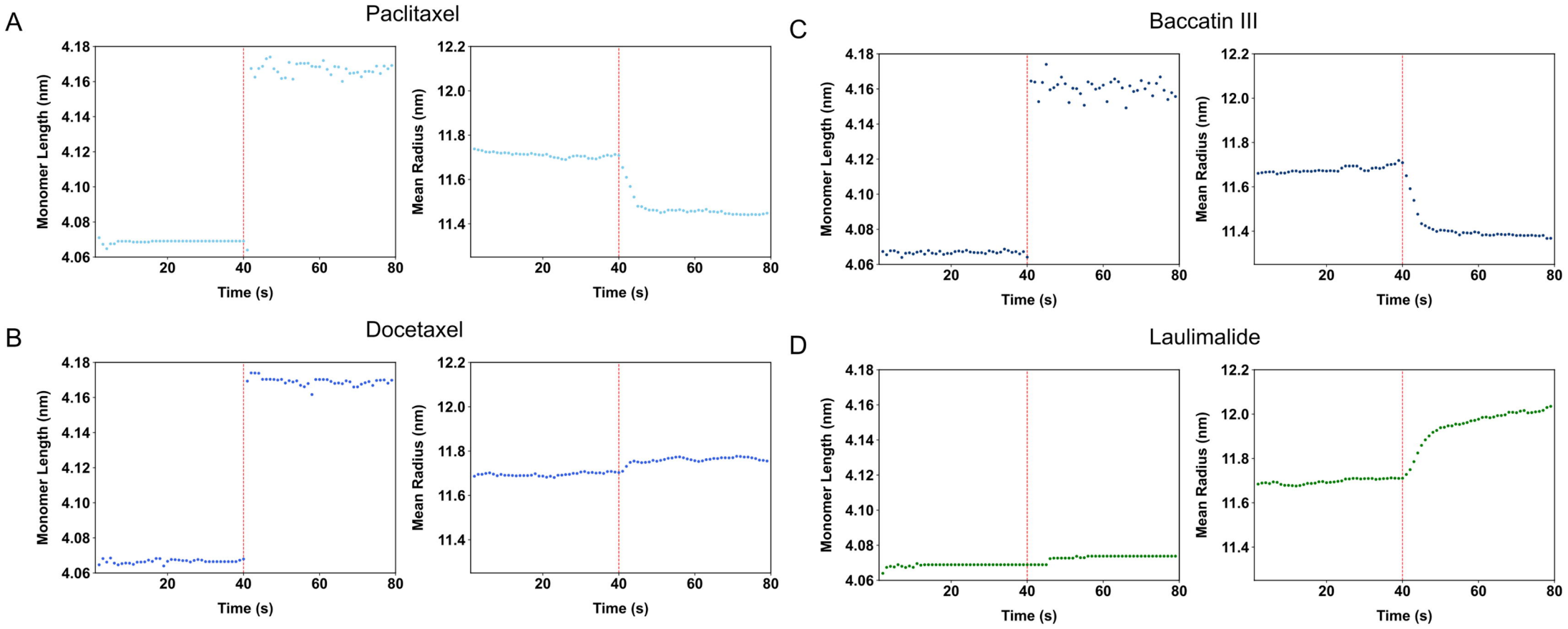
A
Paclitaxel
Monomer Length (nm)
Mean Radius (nm)
Time (s)
B
Docetaxel
C
Baccatin III
D
Laulimalide

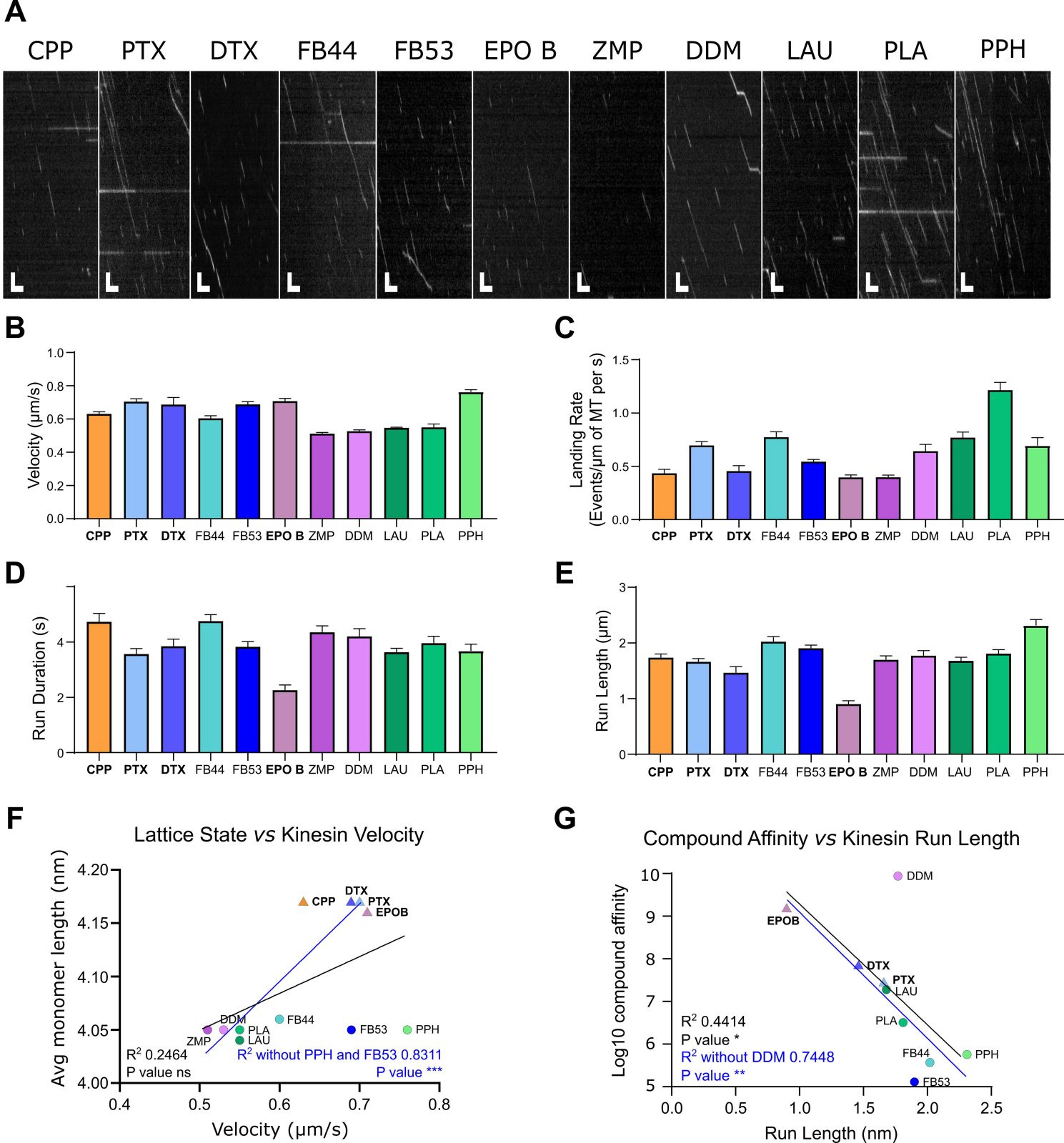
A
CPP
PTX
DTX
FB44
FB53
EPO B
ZMP
DDM
LAU
PLA
PPH
B
Velocity (µm/s)
C
Landing Rate (Events/µm of MT per s)
D
Run Duration (s)
E
Run Length (µm)
F
Lattice State vs Kinesin Velocity
Avg monomer length (nm)
Velocity (µm/s)
R² 0.2464
P value ns
R² without PPH and FB53 0.8311
P value ***
G
Compound Affinity vs Kinesin Run Length
Log10 compound affinity
Run Length (nm)
R² 0.4414
P value *
R² without DDM 0.7448
P value **

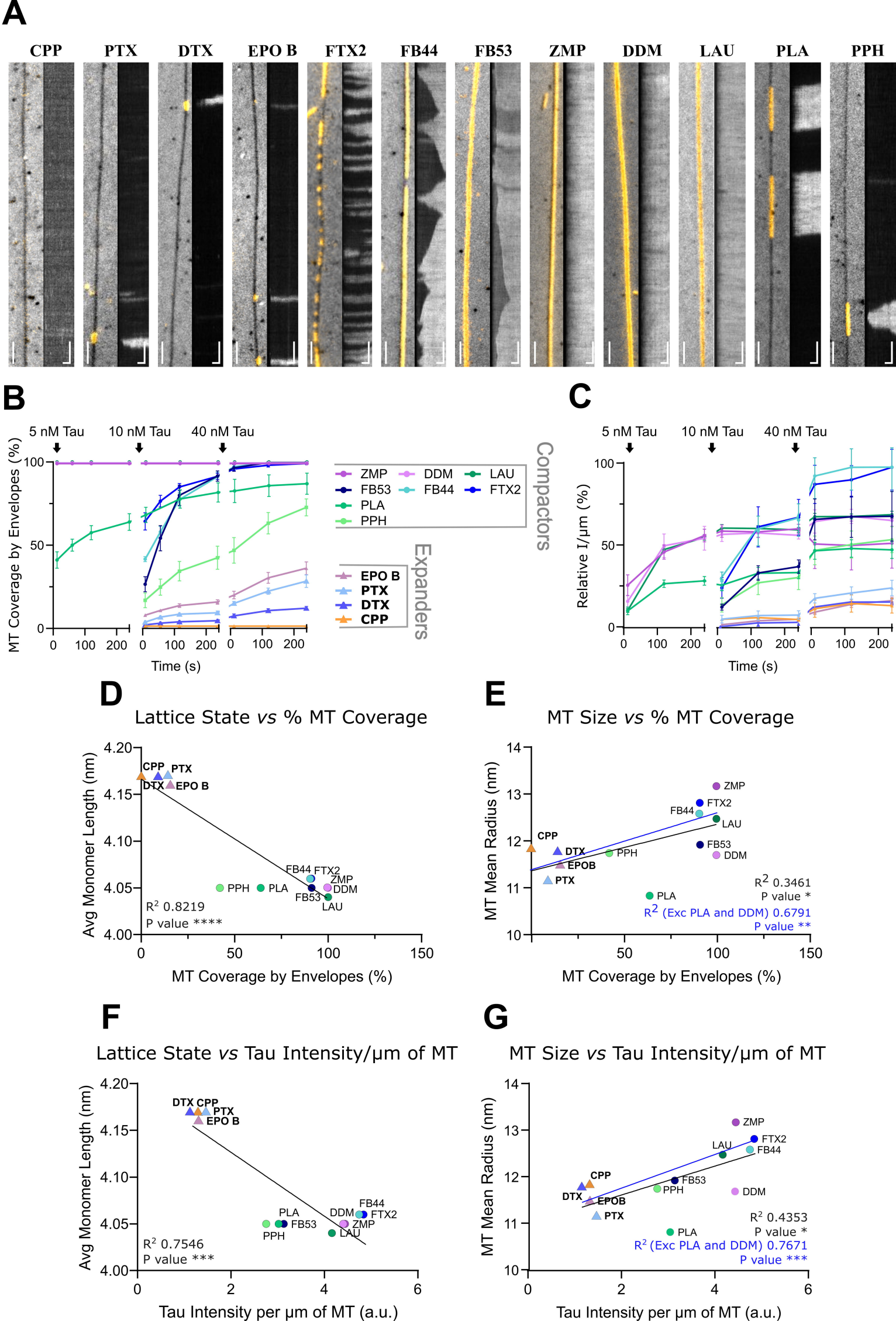
A
CPP
PTX
DTX
EPO B
FTX2
FB44
FB53
ZMP
DDM
LAU
PLA
PPH
B
5 nM Tau
10 nM Tau
40 nM Tau
MT Coverage by Envelopes (%)
Time (s)
ZMP
FB53
PLA
PPH
DDM
FB44
LAU
FTX2
Compactors
EPO B
PTX
DTX
CPP
Expanders
C
Relative I/µm (%)
D
Lattice State vs % MT Coverage
Avg Monomer Length (nm)
MT Coverage by Envelopes (%)
R² 0.8219
P value ****
E
MT Size vs % MT Coverage
MT Mean Radius (nm)
R² 0.3461
P value *
R² (Exc PLA and DDM) 0.6791
P value **
F
Lattice State vs Tau Intensity/µm of MT
Tau Intensity per µm of MT (a.u.)
R² 0.7546
P value ***
G
MT Size vs Tau Intensity/µm of MT
R² 0.4353
P value *
R² (Exc PLA and DDM) 0.7671
P value ***

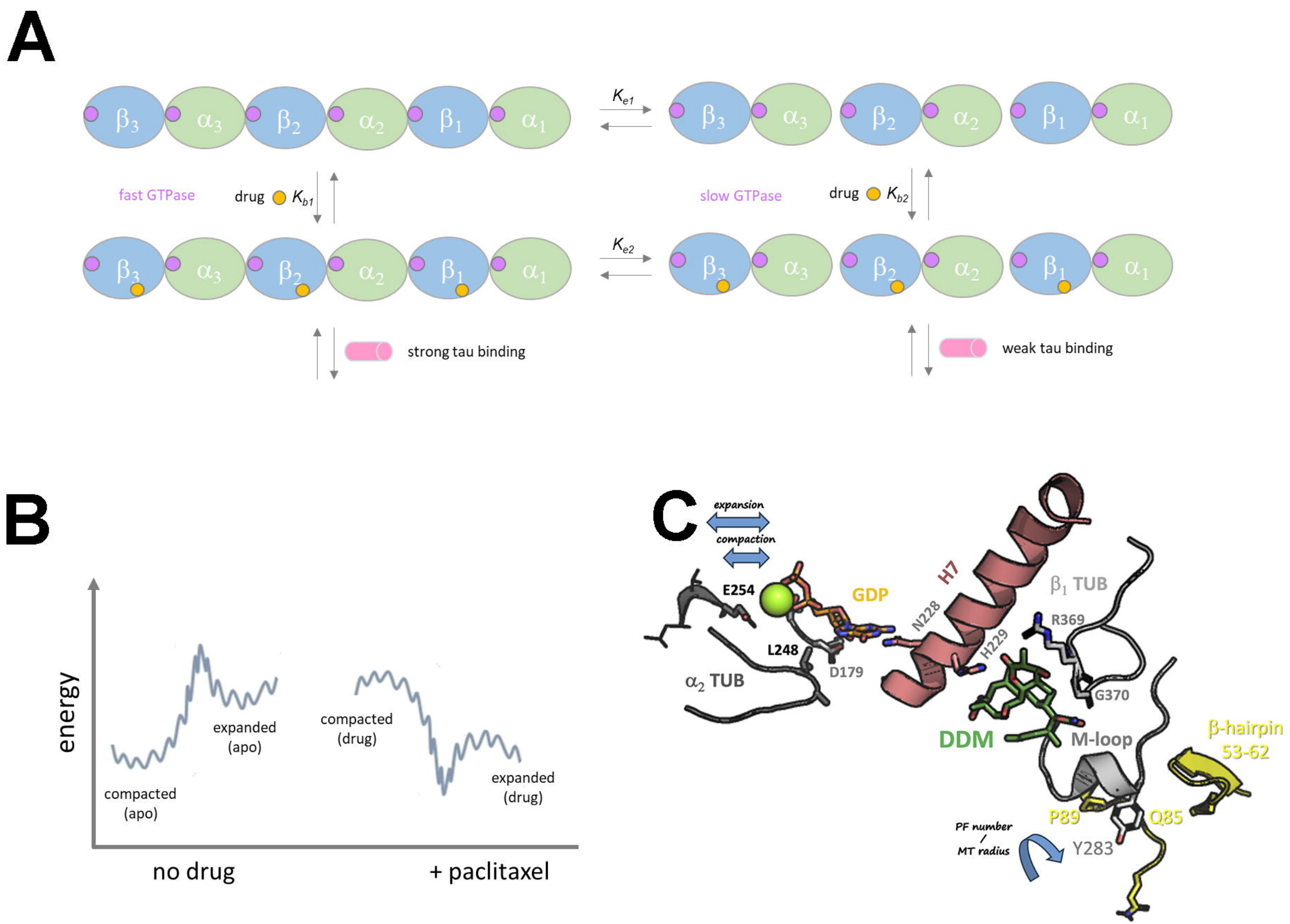
A
β3 α3 β2 α2 β1 α1
Ke1
fast GTPase
drug Kb1
slow GTPase
drug Kb2
Ke2
strong tau binding
weak tau binding
B
energy
compacted (apo)
expanded (apo)
compacted (drug)
expanded (drug)
no drug
+ paclitaxel
C
expansion
compaction
E254
GDP
L248
D179
α2 TUB
H7
N228
H229
β1 TUB
R369
G370
DDM
M-loop
β-hairpin 53-62
P89
Q85
Y283
PF number / MT radius